Acknowledgements

For access to data we thank P. Helm for facilitating data provision; J. Wilesmith for provision of the VLA FMD case data; A. Wray, T. Sharp and M. Horn for providing census and location data; B. Froggatt, S. Newell and P. Swanton for analysing IACS data and providing a database on farmland fragmentation; F. Mallin and J. Moodey for provision of the LW(D)S (Livestock Welfare (Disposal) Scheme) data; and J. Bell and C. Cox for providing CTS (Cattle Tracing System) data. We thank members of the Chief Scientist's advisory group on FMD for discussions. N.M.F. thanks the Royal Society and the Howard Hughes Medical Institute, and C.A.D. and R.M.A. thank the Wellcome Trust for research funding.

Correspondence and requests for materials should be addressed to N.M.F. (e-mail: neil.ferguson@ic.ac.uk).

erratum

The timing of the last deglaciation in North Atlantic climate records

Claire Waelbroeck, Jean-Claude Duplessy, Elisabeth Michel, Laurent Labeyrie, Didier Paillard & Josette Duprat

Nature **412,** 724–727 (2001).

In this Letter, the following line should have appeared before the reference list: "Received 10 November 2000; accepted 5 July 2001.' □

Control of conformational and interpolymer effects in conjugated polymers

J. Kim & M. Swager

Nature **411,** 1030–1034 (2001).

In Fig. 2a the pressure–area isotherms for polymers 2 and 3 were incorrectly labelled as 'Polymer 3' and 'Polymer 2', respectively. □

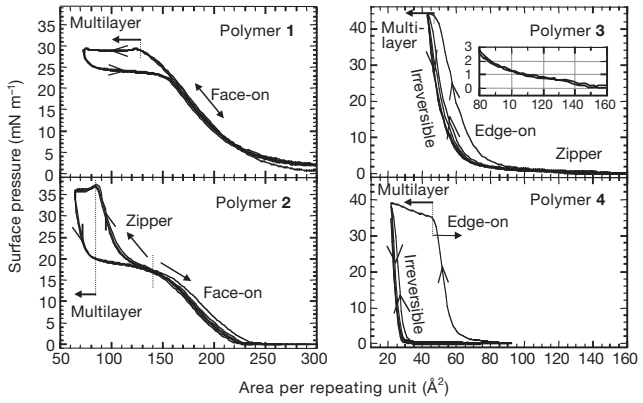

Figure 2a

Partitioning selection and complementarity in biodiversity experiments

Michel Loreau & Andy Hector

Nature **412,** 72–76 (2001).

In Figures 2 and 3, some regression lines were very faint or missing. The corrected panels are reproduced below. All panels in both figures should also have shown the null hypothesis as a horizontal dashed line through zero. □

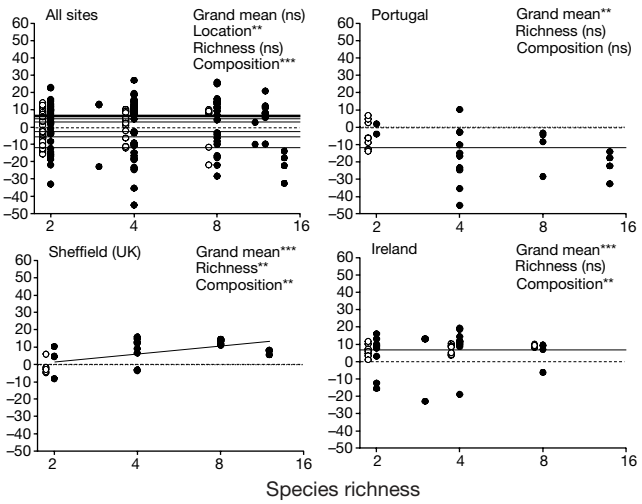

Figure 2

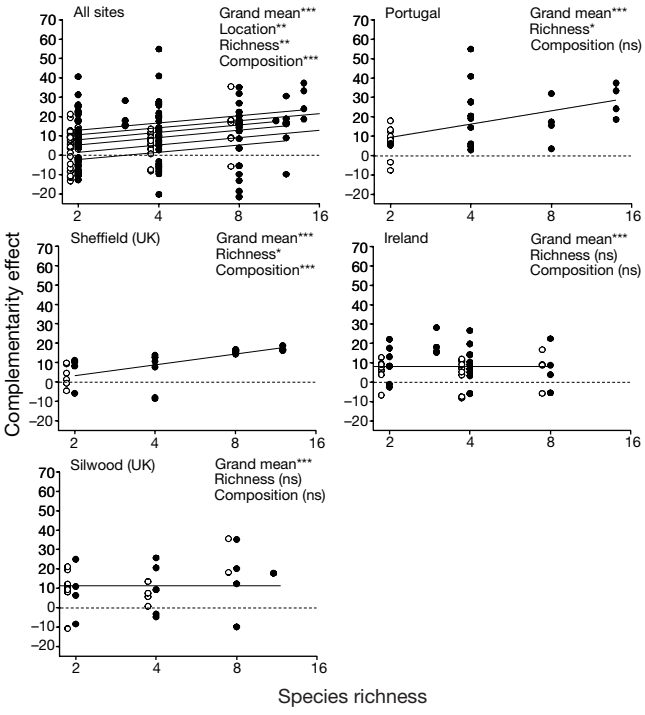

Figure 3

28. Young, R. A. (ed.) *The Rietveld Method* (Oxford Univ. Press, Oxford, 1993).
29. Larson, A. C. & von Dreele, R. B. *GSAS Report LAUR 86-784* (Los Alamos National Laboratory, 1986).
30. Breck, D. W. *Zeolite Molecular Sieves* (Wiley, New York, 1974).
31. Mitariten, M. & Dolan, W. Nitrogen removal from natural gas with molecular gate technology. *Proc. Laurance Reid Gas Cond. Conf.* **51,** 1–16 (2001).
32. Abrams, L. & Corbin, D. R. in *Topics in Inclusion Science* Vol. 6, *Inclusion Chemistry with Zeolites: Nanoscale Materials by Design* (eds Herron, N. & Corbin, D. R.) 4–6 (Kluwer, Dordrecht, 1995).

Supplementary information is available on *Nature*'s World-Wide Web site (http://www.nature.com) or as paper copy from the London editorial office of *Nature*.

Acknowledgements

We thank J. Curran for discussions and assistance in the preparation of the manuscript, and VTI Corp. for the data of Fig. 5. This work was supported by ATP/NIST, the David and Lucile Packard Foundation and NSF-CTS.

Correspondence and requests for materials should be addressed to S.M.K. (e-mail: steve.kuznicki@engelhard.com).

The timing of the last deglaciation in North Atlantic climate records

Claire Waelbroeck*, Jean-Claude Duplessy*, Elisabeth Michel*, Laurent Labeyrie*†, Didier Paillard* & Josette Duprat‡

** Laboratoire des Sciences du Climat et de l'Environnement, Domaine du CNRS, bât. 12, 91198 Gif-sur-Yvette, France*
† Département des Sciences de la Terre, Université Paris-sud Orsay, bât. 504, 91104 Orsay, France
‡ Département de Géologie et Océanographie, CNRS UMR 5805, Université de Bordeaux I, Talence, France

To determine the mechanisms governing the last deglaciation and the sequence of events that lead to deglaciation, it is important to obtain a temporal framework that applies to both continental and marine climate records. Radiocarbon dating has been widely used to derive calendar dates for marine sediments, but it rests on the assumption that the 'apparent age' of surface water (the age of surface water relative to the atmosphere) has remained constant over time[1,2]. Here we present new evidence for variation in the apparent age of surface water (or reservoir age) in the North Atlantic ocean north of 40° N over the past 20,000 years. In two cores we found apparent surface-water ages to be larger than those of today by 1,230 ± 600 and 1,940 ± 750 years at the end of the Heinrich 1 surge event (15,000 years BP) and by 820 ± 430 to 1,010 ± 340 years at the end of the Younger Dryas cold episode. During the warm Bølling–Allerød period, between these two periods of large reservoir ages, apparent surface-water ages were comparable to present values. Our results allow us to reconcile the chronologies from ice cores and the North Atlantic marine records over the entire deglaciation period. Moreover, the data imply that marine carbon dates from the North Atlantic north of 40° N will need to be corrected for these highly variable effects.

The last deglaciation is a period particularly well dated because it belongs to the time span covered by isotopic (^{14}C) dating techniques, which can be applied to both continental and marine sediments. Moreover, ^{14}C dates can be converted into calendar ages through calibration curves describing the variations in the atmospheric $^{14}C/^{12}C$ ratio over the past 20 kyr (ref. 3). Also, the uncertainty on the absolute dating by annual-layer counting of the Greenland ice cores is small (<550 yr) over the last 15 kyr (ref. 4). Therefore, it is possible to compare directly the timing of events from continental and ice-core records, and thus to infer causal mechanisms from the data. The situation is more complex for the marine data, as the ^{14}C dates are measured on foraminifera preserved in the sediments and hence reflect the $^{14}C/^{12}C$ ratio of the water in which the foraminifera calcified. The surface-water $^{14}C/^{12}C$ ratio is different from that of the contemporaneous atmosphere, reflecting the balance between the input of atmospheric ^{14}C and its removal by transport and radiodecay in the water column. This difference in $^{14}C/^{12}C$ ratio is usually expressed as the apparent or reservoir age of the water mass.

A compilation of pre-bomb surface-water ^{14}C content indicates that the modern surface reservoir age is about 400 ± 100 yr in the tropics and in the North Atlantic whereas it rises to 1,200 yr at higher latitudes in the Southern and North Pacific oceans[5,6]. Past reservoir ages most probably differed from those of today, but only sparse data exist. Reservoir ages have been measured in a few sites at given times in the past, by dating contemporaneous samples in marine sediments and in terrestrial organic matter, marked by the same volcanic ash layer[7–10].

Here, we present summer sea surface temperature (SST) reconstructions and benthic oxygen isotopic records ($\delta^{18}O_b$) from three sediment cores raised for the North Atlantic Ocean between 37 and 55° N (SU 81-18, 37° 46′ N, 10° 11′ W, 3,135 m; CH 69-09, 41° 45′ N, 47° 21′ W, 4,100 m; and NA 87-22, 55° 29′ N, 14° 41′ W, 2,161 m). These records have been dated by accelerator mass spectrometry on monospecific planktonic foraminifera samples[1,11,12] (see Supplementary Information Table 1). Radiocarbon ages have been converted into calendar ages with the CALIB 4.1 software[13], the smoothed (310-yr moving average) 1998 marine calibration curve

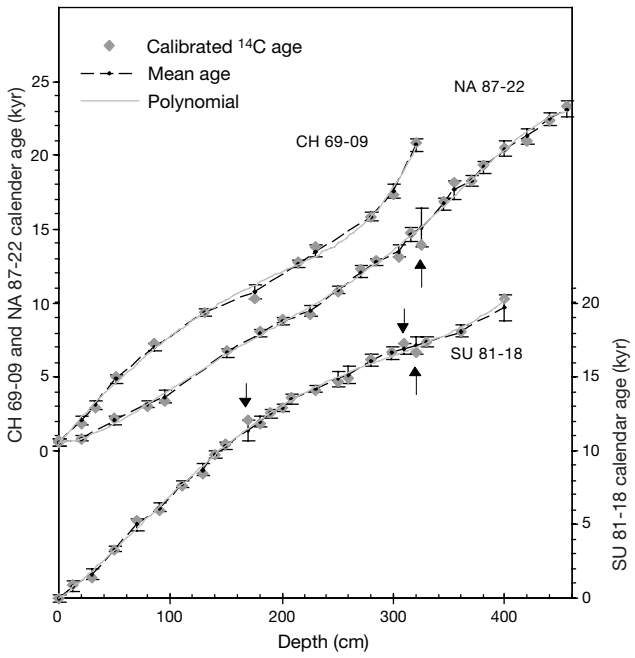

Figure 1 Age–depth relationships for the three North Atlantic deep sea cores. Calendar ages were calculated from the measured ^{14}C ages (see Supplementary Information Table 1) with the CALIB 4.1 software[13] and a constant surface reservoir age of 400 yr. For each core, two different interpolation schemes were used: first, we computed the fifth-order polynomial fitting the dated levels (grey line); second, we linearly interpolated the dated levels, leaving out one age in core NA 87-22 and three ages in core SU 81-18 that showed small age inversions (arrows). The error on the linearly interpolated age scale is taken as one standard deviation of the sample's calendar-age probability distribution given by CALIB 4.1. The error on the polynomial age scale is taken as the difference between the actual sample calendar age and the polynomial age computed at the same level, when this difference is larger than the error on the sample's calendar age. It is otherwise equal to the error on the linearly interpolated age scale. We derived the final age model for each core (black dots with 1-s.d. error bars) by taking the arithmetical mean of the above two timescales to ensure realistically large error bars. The final error estimate includes an additional 200-yr uncertainty, representing the maximum possible bioturbation bias. Both interpolation schemes support our conclusions.

of Stuiver *et al.*[3], and a constant surface reservoir age of 400 yr (Fig. 1). The method provides the probability distribution of the sample's calendar age.

The sedimentation rate is about 20 cm kyr^{-1} between 10 and 15 kyr before present (BP) for the three cores examined here (Fig. 1). Therefore, bioturbation should not induce significant biases[14]. Moreover, the ^{14}C ages were determined on planktonic monospecific samples selected in the species abundance maxima (see Supplementary Information Table 1), so that bioturbation distortion of the above dating is minimized.

The three North Atlantic SST series can now be plotted against calendar age, together with the GRIP or GISP2 ice–oxygen isotopic record, a proxy for air temperature[15] (Fig. 2). All three SST series depict a clear two-step warming of 7–12 °C amplitude from the end of the last glacial to the Holocene. The first warming phase is extremely abrupt, as can be seen in the two records of highest resolution (CH 69-09 and SU 81-18) and corresponds to GRIP's sharp increase in air temperature marking the transition between the last Heinrich event (H1) (ref. 16) and the Bølling–Allerød interval. Similarly, the second rapid-warming phase should correspond with the transition from the Younger Dryas cold episode to the Holocene.

Assuming a constant surface reservoir age implies very large leads of the SST increase at the two northernmost Atlantic sites with respect to the increase in air temperature above Greenland. These leads can be accurately evaluated (see Supplementary Information Table 2), with the total uncertainty on the warming-midpoint dates resulting from the error related to the time resolution and from the dating error (Fig. 1). The first sharp SST increase is found to lead the H1–Bølling–Allerød transition recorded in the Greenland ice by 1.94 ± 0.75 kyr in core NA 87-22, and by 1.23 ± 0.60 kyr in core CH 69-09. Similarly, the second abrupt SST increase leads the Younger Dryas–Holocene transition in the ice by 0.82 ± 0.43 kyr in core NA 87-22, and 1.01 ± 0.34 kyr in core CH 69-09. In contrast, the SST variations recorded in core SU 81-18, located further south (38° N), coincide with air temperature variations above Greenland.

Several lines of evidence drive us to conclude that the large leads observed in the northernmost records are not real climatic features. First, examining the marine $\delta^{18}O_b$ records reveals a similar significant lead of the decrease in $\delta_{18}O_b$ associated with the deglaciation in the northern records compared with the SU 81-18 mid-latitudes $\delta^{18}O_b$ record (Fig. 3a). The decrease in $\delta^{18}O_b$ taking place during deglaciations results from the combined effect of ice melting and deep-water warming. Because the three cores are geographically relatively close and bathed by water masses dominated by North Atlantic deep water (NADW), large changes in $\delta^{18}O_b$ should take place roughly simultaneously at the three locations. Therefore, a different timing of the warming cannot explain the lead of 1–2 kyr

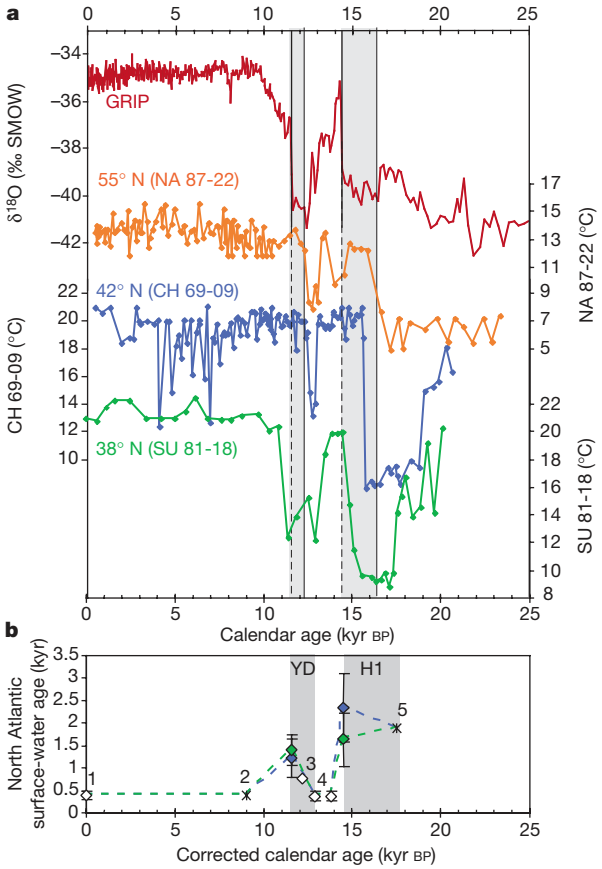

Figure 2 Surface temperature records and reconstructed evolution of the surface reservoir age during the last 18 kyr. **a**, Comparison of GRIP ice $\delta^{18}O$ (a proxy for air temperature) and summer SST reconstructions at the three North Atlantic sites versus calendar age. SST has been reconstructed from the planktonic foraminifera abundances by the revised analogue method[27,28]. Grey stripes highlight the large leads between NA 87-22 SST and GRIP air temperature at the H1–Bølling–Allerød and Younger Dryas–Holocene transitions. **b**, Tentative synthesis of variations in surface-water ages in the North Atlantic north of 40° N during the last 18 kyr. Filled diamonds, our results; unfilled diamonds, estimates available in the literature: 1, pre-bomb value[5,6]; 3, reservoir ages obtained by dating of the Vedde ash layer[7,8]; 4, Bølling–Allerød reservoir ages measured in Norwegian coastal waters[29]. Crosses, possible additional constraints: 2, ocean circulation in the North Atlantic can be considered as similar to today around 9 kyr BP (ref. 20); 5, approximate value derived from the difference between the initiation of the cooling associated with H1 in SU 81-18 and in CH 69-09, assuming a reservoir age of 0.4 kyr at the SU 81-18 site. Dotted line, proposed evolution of surface-water age at high latitudes in the North Atlantic.

of the northern $\delta^{18}O_b$ records with respect to the $\delta^{18}O_b$ signal of core SU 81-18. The lead of the northern records with respect to the mid-latitudes record seems thus to be an artefact of the ^{14}C chronology.

Second, no reasonable climatic mechanism can explain how SST at site NA 87-22, located in the same latitude band as Greenland, could have reached interglacial values 0.8–1.9 kyr before the SST off Portugal (site SU 81-18) and the air temperature above Greenland.

On the contrary, we have reasons to believe that the small surface-water ages currently observed in the North Atlantic did not prevail in the past. In fact, current constant reservoir ages over the North Atlantic are principally due to the North Atlantic Drift, which brings low-latitude surface waters to 50–60° N and into the Norwegian Sea. The cooling of warm and saline surface waters at high latitudes induces active deep-water formation in these areas, associated with a large flux of atmospheric ^{14}C to the surface waters. Consequently, the presence of large continental ice caps, the southward shift of the polar front and the associated shift in deep-water-formation areas during the Younger Dryas cold episode and the last glacial maximum[17–21] probably explain an important decrease in ventilation and hence an increase in surface-water reservoir age, north of the polar front[7]. It was also demonstrated that iceberg discharge H1 had a large impact on ocean circulation, further reducing NADW formation[20,22].

The effect of circulation changes on the ocean radiocarbon content has been evaluated with coupled ocean–ice–atmosphere models[23–25]. These modelling experiments show that a reduction in NADW overturn and an increase in sea ice cover lead to an increase in surface-water age of 200–300 yr in the Atlantic, north of 40° N. These results are thus consistent with our findings, although the increase in surface reservoir age predicted by the models is weaker than our data indicate. This seems to result from the fact that these models simulate no or very little vertical convection north of the polar front, although palaeoceanographic data show the opposite[26].

The two northernmost cores demonstrated leads of the SST abrupt warmings with respect to the air temperature increases recorded in the Greenland ice. We interpret these leads as increases in the surface reservoir age at the cores' location during these two specific climatic transitions. A tentative reconstruction of the evolution of the Atlantic surface-water age during the last 18 kyr can be derived from the compilation of available estimates of apparent surface-water ages (Fig. 2b). After correcting the marine time scales to account for these large reservoir ages, the three $\delta^{18}O_b$ records are in much better agreement between 11 and 18 kyr (Fig. 3b), the residual differences probably resulting from measurement uncertainties, noise due to bioturbation, and small differences in deep water temperature variations between sites.

This study allowed us to reconcile ice core and North Atlantic marine chronologies, as well as surface and deep-water climatic records from mid- to high latitudes, over the entire deglaciation period. We demonstrated that the surface-water age at high latitudes in the North Atlantic has varied by a factor of 3–5 during the past 15 kyr, owing presumably to major changes in ocean circulation and sea ice cover. It is therefore highly probable that it also significantly varied across the Heinrich and Dansgaard–Oeschger climatic events of the last glacial period (see for example ref. 2), inducing biases in marine ^{14}C chronologies. The situation at high southern latitudes is expected to be similar, as indicated by recent measurements showing large increases in surface reservoir ages in the New Zealand region during glacial times[10]. □

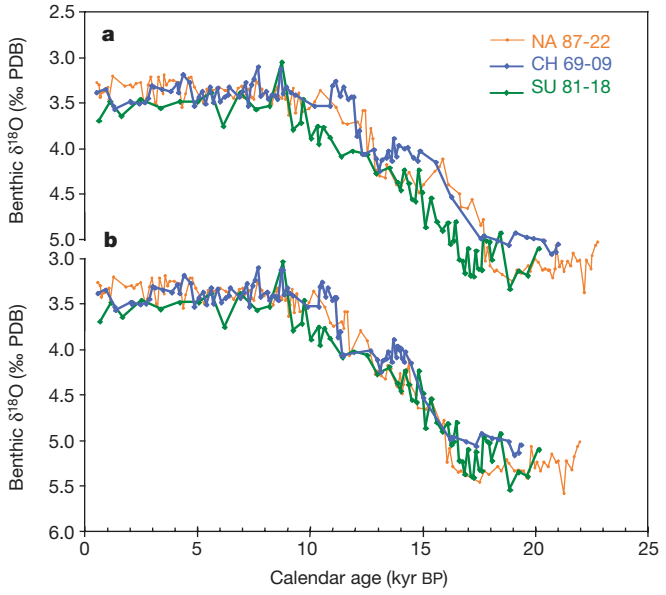

Figure 3 $\delta^{18}O_b$ records from the three North Atlantic cores. Data[11,12,30] are expressed in ‰ versus the Pee Dee Belemnite (PDB) standard. **a**, Records versus the calendar-age scale defined in Fig. 1. **b**, Same records after correcting the original age scale to account for the variations in surface-water age according to our tentative synthesis (Fig. 2b).

1. Bard, E. *et al.* Retreat velocity of the North Atlantic polar front during the last deglaciation determined by ^{14}C accelerator mass spectrometry. *Nature* **328,** 791–794 (1987).
2. Voelker, A. *et al.* Correlation of marine ^{14}C ages from the Nordic Seas with the GISP2 isotope record: Implications for ^{14}C calibration beyond 25 ka BP. *Radiocarbon* **40,** 517–534 (1998).
3. Stuiver, M. *et al.* INTCAL98 radiocarbon age calibration, 24,000-0 cal BP. *Radiocarbon* **40,** 1041–1083 (1998).
4. Alley, R. B. *et al.* Abrupt increase in Greenland snow accumulation at the end of the Younger Dryas event. *Nature* **362,** 527–529 (1993).
5. Bard, E. Correction of accelerator mass spectrometry ^{14}C ages measured in planktonic foraminifera: paleoceanographic implications. *Paleoceanography* **3,** 635–645 (1988).
6. Stuiver, M. & Braziunas, T. F. Sun, ocean, climate and atmospheric $^{14}CO_2$: an evaluation of causal and spectral relationship. *The Holocene* **3,** 289–305 (1993).
7. Bard, E. *et al.* The North Atlantic atmosphere-sea surface ^{14}C gradient during the Younger Dryas climatic event. *Earth Planet. Sci. Lett.* **126,** 275–287 (1994).
8. Austin, W. E. N., Bard, E., Hunt, J. B., Kroon, D. & Peacock, J. D. The ^{14}C age of the Icelandic Vedde Ash: implications for Younger Dryas marine reservoir age corrections. *Radiocarbon* **37,** 53–62 (1995).
9. Siani, G. *Estimation de l'âge ^{14}C du réservoir des eaux de surface de la mer Méditerranée pendant les derniers 18000 ans.* Thesis, Univ. Paris-Sud (1999).
10. Sikes, E. L., Samson, C. R., Guilderson, T. P. & Howard, W. R. Old radiocarbon ages in the southwest Pacific Ocean during the last glacial period and deglaciation. *Nature* **405,** 555–559 (2000).
11. Duplessy, J. C. *et al.* Changes in surface salinity of the North Atlantic Ocean during the last deglaciation. *Nature* **358,** 485–487 (1992).
12. Labeyrie, L. *et al.* in *Mechanisms of Global Climate Change at Millennial Time Scales, Geophysical Monograph Series 112* (eds Clark, P. & Webb, R. S.) 77–98 (American Geophysical Union, Washington, DC, 1999).
13. Stuiver, M. & Reimer, P. J. Extended ^{14}C data base and revised CALIB 3.0 ^{14}C age calibration program. *Radiocarbon* **35,** 215–230 (1993).
14. Bard, E., Arnold, M., Duprat, J., Moyes, J. & Duplessy, J. C. Reconstruction of the last deglaciation: deconvolved records of $\delta^{18}O$ profiles, micropaleontological variations and accelerator mass spectrometric ^{14}C dating. *Clim. Dynam.* **1,** 101–112 (1987).
15. Johnsen, S. J. *et al.* The $\delta^{18}O$ record along the Greenland Ice Core Project deep ice core and the problem of possible Eemian climatic instability. *J. Geophys. Res.* **102,** 26397–26410 (1997).
16. Broecker, W., Bond, G., Klas, M., Clark, E. & MacManus, J. Origin of the northern Atlantic's Heinrich events. *Clim. Dynam.* **6,** 265–273 (1992).
17. Boyle, E. A. Cadmium: chemical tracer deepwater paleoceanography. *Paleoceanography* **3,** 471–489 (1988).
18. Labeyrie, L. D. *et al.* Changes in vertical structure of the North Atlantic Ocean between glacial and modern times. *Quat. Sci. Rev.* **11,** 401–413 (1992).
19. Duplessy, J.-C. *et al.* Deepwater source variations during the last climatic cycle and their impact on the global deepwater circulation. *Paleoceanography* **3,** 343–360 (1988).
20. Sarnthein, M. *et al.* Changes in east Atlantic deepwater circulation over the last 30,000 years: eight time slice reconstructions. *Paleoceanography* **9,** 209–267 (1994).
21. Muscheler, R., Beer, J., Wagner, G. & Finkel, R. Changes in deep-water formation during the Younger Dryas event inferred from ^{10}Be and ^{14}C records. *Nature* **408,** 567–570 (2000).
22. Vidal, L. *et al.* Evidence for changes in the North Atlantic Deep Water linked to meltwater surges during the Heinrich events. *Earth Planet. Sci. Lett.* **146,** 13–26 (1997).
23. Mikolajewicz, U. A meltwater induced collapse of the conveyor belt thermohaline circulation and its influence on the distribution of $\Delta^{14}C$ and $\delta^{18}O$ in the oceans. *Max Planck Inst. Rep.* **189,** 1–25 (1996).
24. Stocker, T. F. & Wright, D. G. Rapid changes in ocean circulation and atmospheric radiocarbon. *Paleoceanography* **11,** 773–795 (1996).
25. Stocker, T. F. & Wright, D. G. The effect of a succession of ocean ventilation changes on ^{14}C. *Radiocarbon* **40,** 359–366 (1998).
26. Dokken, T. M. & Jansen, E. Rapid changes in the mechanism of ocean convection during the last glacial period. *Nature* **401,** 458–461 (1999).
27. Waelbroeck, C. *et al.* Improving past sea surface temperature estimates based on planktonic fossil faunas. *Paleoceanography* **13,** 272–283 (1998).

28. Malmgren, B., Kucera, M., Nyberg, J. & Waelbroeck, C. Comparison of available statistical and artificial neural network techniques for estimating past sea-surface temperatures from planktonic foraminifera census data. *Palaeoceanography* (in the press).
29. Bondevik, S., Birks, H. H., Gulliksen, S. & Mangerud, J. Late Weichselian marine ^{14}C reservoir ages at the western coast of Norway. *Quat. Res.* **52,** 104–114 (1999).
30. Labeyrie, L. *et al.* Surface and deep hydrology of the northern Atlantic Ocean during the last 150,000 years. *Phil. Trans. R. Soc. Lond.* **348,** 255–264 (1995).

Supplementary information is available on *Nature*'s World-Wide Web site (http://www.nature.com) or as paper copy from the London editorial office of *Nature*.

Acknowledgements

We thank E. Bard and G. Siani for discussions and comments. The data were acquired in collaboration with T. van Weering, J.-L. Turon, M. Labracherie and G. Auffret. We thank B. Lecoat and J. Tessier for processing the isotopic measurements. This study was supported by CNRS, CEA, INSU (PNEDC) and EU Environment Program.

Correspondence and requests for materials should be addressed to C.W. (e-mail: Claire.Waelbroeck@lsce.cnrs-gif.fr).

Direct observation of a submarine volcanic eruption from a sea-floor instrument caught in a lava flow

Christopher G. Fox*†, William W. Chadwick Jr†‡ & Robert W. Embley*

* *NOAA/PMEL, Newport, Oregon 97365, USA*
‡ *2115 SE OSU Drive, Oregon State University/NOAA, Newport, Oregon 97365, USA*
† *These authors contributed equally to this work*

Our understanding of submarine volcanic eruptions has improved substantially in the past decade owing to the recent ability to remotely detect such events[1] and to then respond rapidly with synoptic surveys and sampling at the eruption site. But these data are necessarily limited to observations after the event[2]. In contrast, the 1998 eruption of Axial volcano on the Juan de Fuca ridge[3,4] was monitored by *in situ* sea-floor instruments[5–7]. One of these instruments, which measured bottom pressure as a proxy for vertical deformation of the sea floor, was overrun and entrapped by the 1998 lava flow. The instrument survived—being insulated from the molten lava by the solidified crust—and was later recovered. The data serendipitously recorded by this instrument reveal the duration, character and effusion rate of a sheet flow eruption on a mid-ocean ridge, and document over three metres of lava-flow inflation and subsequent drain-back. After the brief two-hour eruption, the instrument also measured gradual subsidence of 1.4 metres over the next several days, reflecting deflation of the entire volcano summit as magma moved into the adjacent rift zone. These findings are consistent with our understanding of submarine lava effusion, as previously inferred from seafloor observations, terrestrial analogues, and laboratory simulations[8–11].

Two Volcanic System Monitor (VSM) instruments were deployed at Axial volcano in October 1997, one near the centre of the caldera[5] and one on the upper south rift zone, hereafter referred to as VSM1 and VSM2, respectively (Figs 1 and 2). The VSM instruments measure ambient pressure on the sea floor every 15 s with a Paroscientific digiquartz pressure sensor. The data processing methods are described in detail elsewhere[5,12], but include filtering to remove oceanographic phenomena and a correction for temperature. In August 1998, VSM2 was found to be trapped in the new lava flow (Fig. 1), but it was pulled free the following summer.

The rescued instrument was in surprisingly good condition. The maximum temperature recorded inside VSM2 during the eruption was only 7.5 °C (Fig. 3)—remarkably low, considering that the instrument was sitting atop basaltic lava that was probably erupted at ~1,190 °C (M. Perfit, personal communication). This was apparently due to the thermal insulation provided by the surface crust that forms (and quickly thickens) when submarine lava flows come into contact with frigid sea water[13].

The northern end of the 1998 lava flow where VSM2 was located (Fig. 2) is a long, narrow sheet flow[4]. Submarine sheet flows are thought to form by brief, relatively high-effusion-rate eruptions[8,9]. Recent models[10,11] suggest that such flows initially advance as thin lobate flows (20–30 cm thick), spreading at a rate that is rapid enough for the interior of the flow to remain a single fluid core beneath a solid upper crust. The flow spreads until it becomes laterally confined, and then 'inflates' upward. During inflation, the upper crust is uplifted (sometimes > 5 m) by hydraulic pressure within the flow interior—and lava pillars grow upward, connecting the upper and lower crusts[10]. Lava inflation continues until the eruption rate wanes or stops, at which point lava begins to drain back and the upper crust founders where it is left unsupported, leaving extensive areas of collapse within the flow.

Geologic mapping of the 1998 lava flow shows that VSM2 was located in the collapsed interior of the 1998 lava flow, ~3 m below nearby remnants of the uncollapsed upper crust and ~160 m west of the eruptive fissure (Fig. 2). The instrument had not been buried by lava, even though the lava level had been 3 m higher before collapse. This observation implies that lava initially flowed under the instrument, which became embedded in the upper crust of the flow when the flow subsequently inflated. During inflation, VSM2 was uplifted along with the upper crust (because of its table-like design) and then was set back down within the collapse area during the drain-back stage.

The dataset recovered from the VSM2 instrument directly recorded this sequence of events (Fig. 3). Uplift of the instrument began slowly at 14:55 on 25 January 1998 (all times GMT), after the onset of the earthquake swarm at 11:33 (ref. 3) and subsidence began at VSM1 at 14:51 (ref. 5). Rapid inflation abruptly started at 15:16 when VSM2 was uplifted 168 cm in the next 5 minutes, an average rate of 32 cm min^{-1} (although instantaneous rates were as high as 73 cm min^{-1}). After a pause of 4 minutes, during which the instrument subsided 13 cm, inflation resumed for another 21 minutes which uplifted the instrument another 113 cm at a decreased rate of 5.5 cm min^{-1}. At 15:46, inflation dramatically slowed, probably owing to a sudden reduction in the effusion rate at the vent, and the instrument was only uplifted another 7 cm over the next 21 minutes. During this period the lava flow remained at or near its fully inflated thickness, and the recorded temperature reached its peak of 7.5 °C at 15:49 (Fig. 3).

At this point, lava inflation ended and lava drain-back began, presumably reflecting the end of lava effusion at the vent. Our

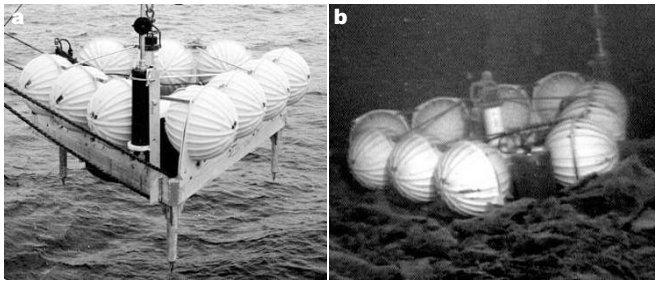

Figure 1 Views of the VSM2 instrument. **a**, At the surface during deployment (legs are 46 cm long), and **b**, on the sea floor, stuck in the 1998 lava flow at Axial volcano. Virtual animations and video clips of VSM2 (referred to as a 'rumbleometer') on the sea floor are available at http://www.pmel. noaa.gov/vents/nemo/explorer/rumble.html

except to a small extent through loss of power out of band. However, noise photons injected by the amplifiers and random photon deletion due to absorption cause the propagating field to acquire a stochastic component, which also leads to multiplicative noise effects through the nonlinear term. This leads us to believe that the single-user case will qualitatively exhibit the same decline in spectral efficiency with intensity as the multi-user case. The same qualitative arguments apply to interposing optical phase conjugation elements for nonlinear compensation; fibre absorption and amplifier noise can still be shown to cause multiplicative noise through the cubic term. It would be incorrect to conclude that nonlinearities must always impair capacity: signal regenerators are an obvious conter-example. However, the fundamental insight in the current work is that in nonlinear propagation channels, qualitatively new phenomena that arise from multiplicative noise effects can severely degrade capacity. □

Methods

Gaussian bound to the channel capacity

Proof of the inequality $I(X_G, Y) \geqslant I(X_G, Y_G)$: define $p(X, Y)$ as the product $p_G(X)p(Y|X)$, and $p_G(X, Y)$ to be the joint gaussian distribution having the same second moments as $p(X, Y)$. Also define $p_G(Y)$ to be the corresponding marginal of $p_G(X, Y)$.

$$I(X_G, Y) = \int dX dY p(X, Y) \log\left(\frac{p(X, Y)}{p_G(X)p(Y)}\right) \quad (4)$$

$$= \int dX dY p(X, Y)\left[\log\left(\frac{p_G(X, Y)}{p_G(X)p_G(Y)}\right) - \log\left(\frac{p_G(X, Y)p_G(Y)}{p(X, Y)p_G(X)}\right)\right] \quad (5)$$

As $p(X, Y)$ and $p_G(X, Y)$ share second moments, the first term on the right-hand side is $I(X_G, Y_G)$. The second term may be simplified using the convexity of the logarithm, $\langle\log(f)\rangle \leqslant \log(\langle f\rangle)$ to obtain

$$I(X_G, Y) \geqslant I(X_G, Y_G) - \log\left[\int dX dY p_G(X, Y)\frac{p(Y)}{p_G(Y)}\right] \quad (6)$$

$$\geqslant I(X_G, Y_G). \quad (7)$$

The second inequality follows by first performing the integral over X, and noting that $\log(\int dY p(Y)) = \log(1) = 0$.

Derivation of the average propagator $\langle U\rangle$

This can be done by resumming the perturbation series exactly for $\langle U\rangle$, for delta-correlated $V(z, t)$. Alternatively, using path integrals[7], $\langle U(t, t'; L)\rangle = U_0(t - t'; L)\langle\langle\exp(i\int_0^L dz V(z, t(z)))\rangle\rangle$, where the average is taken over V as well as over paths $t(z)$ satisfying $t(0) = t$, $t(L) = t'$. The result in the text follows by performing the gaussian average over V. Because $\phi = \int_0^L dz V(z, t(z))$ is a linear combination of gaussian variables, it is also gaussian-distributed and satisfies $\langle\exp(i\phi)\rangle = \exp(-\langle\phi^2\rangle/2)$. The result follows by noting that for delta-correlated V, $\langle\phi^2\rangle$ is a constant given by ηL. The delta correlations need to be treated carefully; this can be done by smearing the delta functions slightly and leads to the definition of η given earlier in the text.

Received 13 November 2000; accepted 19 April 2001.

1. Shannon, C. E. A mathematical theory of communications. *Bell Syst. Tech. J.* **27,** 379–423, 623–656 (1948).
2. Biglieri, E., Proakis, J. & Shamai, S. Fading channels: Information-theoretic and communications aspects. *Inform. Theory Trans.* **44,** 2619–2692 (1998).
3. Kogelnik, H. High-capacity optical communication. *IEEE Sel. Topics Quant. Elec.* **6**(6), 1279 (2000).
4. Agrawal, G. P. *Nonlinear Fiber Optics* (Academic, San Diego, 1995).
5. Desurvire, E. *Erbium Doped Fibre Amplifiers* 69 (Wiley, New York, 1994).
6. Cover, T. M. & Thomas, J. A. *Information Theory* 374–458 (Wiley, New York, 1991).
7. Feynman, R. P. & Hibbs, R. A. *Quantum Mechanics and Path Integrals* (McGraw-Hill, New York, 1963).

Acknowledgements

We gratefully acknowledge extensive discussions with E. Telatar, and also with A. Green, P. B. Littlewood, R. Slusher, A. Chraplyvy and G. Foschini. We thank M. Povinelli and L. Wegener for performing numerical and analytical computations to verify the considerations in this Letter, and D. R. Hamann and R. Slusher for careful readings of the manuscript.

Correspondence and requests for materials should be addressed to P.P.M. (e-mail: pmitra@bell-labs.com).

Control of conformational and interpolymer effects in conjugated polymers

J. Kim*† **& T. M. Swager**‡†

* *Department of Materials Science and Engineering,* † *Center for Materials Science and Engineering, and* ‡ *Department of Chemistry, Massachusetts Institute of Technology, Cambridge, Massachusetts 02139, USA*

The role of conjugated polymers in emerging electronic, sensor and display technologies is rapidly expanding. In spite of extensive investigations[1–11], the intrinsic spectroscopic properties of conjugated polymers in precise conformational and spatial arrangements have remained elusive. The difficulties of obtaining such information are endemic to polymers, which often resist assembly into single crystals or organized structures owing to entropic and polydispersity considerations. Here we show that the conformation of individual polymers and interpolymer interactions in conjugated polymers can be controlled through the use of designed surfactant poly(*p*-phenylene-ethynylene) Langmuir films. We show that by mechanically inducing reversible conformational changes of these Langmuir monolayers, we can obtain the precise interrelationship of the intrinsic optical properties of a conjugated polymer and a single chain's conformation and/or interpolymer interactions. This method for controlling the structure of conjugated polymers and establishing their intrinsic spectroscopic properties should permit a more comprehensive understanding of fluorescent conjugated materials.

We designed and synthesized (see Supplementary Information for details) four poly(*p*-phenylene-ethynylene) compounds (PPEs) using four surfactant 'building blocks' that display preferential orientations at the air–water interface. Unique combinations of these building blocks (A–D in Fig. 1) allow us to control an isolated polymer chain's conformation and interpolymer interactions. Building block A, with two *para*-hydrophobic dioctylamide groups, is expected to display a face-on structure, with its phenyl groups co-facial to the air–water interface[12,13]. B has two *para*-hydrophilic triethyleneoxide groups, and is also expected to prefer a face-on structure. The third building block, C, has one hydrophobic and one hydrophilic group *para* to each other, and is inclined towards an equilibrium edge-on structure with the π-plane normal to the interface. The last block, D, with two *ortho*-hydrophobic dodecyloxy groups, favours an edge-on structure. By design we have used these four building blocks to produce PPEs with precise structural features at the air–water interface. As we will show below, these polymers display one of three equilibrium organizations—face-on, alternating face-on and edge-on (zipper), or edge-on—depending upon the structure and surface pressure (Fig. 1).

Central to our analysis is the ability to switch between different structures, by applying mechanical force while monitoring the Langmuir monolayer's optical spectra. Figure 1 shows the chemical structures, conformations and spatial arrangements at the air–water interface of the PPEs. Our assignments of the conformations and spatial arrangements are based on a self-consistent analysis of the pressure–area (P–A) isotherms (Fig. 2a), *in situ* ultraviolet–visible (UV–vis.) and fluorescence spectroscopy (Fig. 3), and molecular modelling (Fig. 2b). Polymer **1** favours the face-on structure with a large extrapolated area per repeating unit of 240 Å^2. As the monolayer is compressed, the surface pressure increases until the monolayer folds into multilayers at 30 mN m^{-1} with an area per repeating unit of 130 Å^2. Molecular modelling predicts a repeating unit area of 126 Å^2 when **1** is highly compressed in the face-on structure (Fig. 2b). The wavelength of maximum

absorption (λ_{max}) of **1** at the air–water interface at 0 mN m^{-1} is red-shifted by 35 nm relative to its solution value owing to the increased π-conjugation length in the face-on structure[5,14]. Our studies point to the polymer having a highly non-planar structure in solution (see below). Compression perturbs the π-conjugation system, causing the blue shift in absorption spectra with increased pressure (Fig. 3a). During the compression, the fluorescence quantum yield is unchanged, indicating—as expected—that edge-to-edge interpolymer interactions do not affect the quantum yield (Fig. 3b). After the monolayer of **1** folds into a multilayer at 30 mN m^{-1}, aggregated fibrils are visually observed. *In situ* UV–vis. spectroscopy also shows an additional aggregation peak at 464 nm, 13 nm to the red of the absorption λ_{max} of the face-on structure with the maximized π-conjugation. We confirmed that the 464-nm band is the result of interpolymer co-facial π–π interactions by conducting the same *in situ* UV–vis. experiment on a previously studied polymer[15] that is isostructural except that the ethylene oxide side chains of B are part of a macrocycle that prevents strong interchain electronic interactions. In this case, even after the folding into a multilayer, the UV–vis. spectrum does not show the aggregation peak at 464 nm. We note that the polymer conformation in the aggregated state probably exhibits an extended conjugation, which will facilitate the strong interpolymer electronic interactions. The P–A isotherm of **1** is completely reversible, as are the spectroscopic changes.

Polymer **2** also shows completely reversible P–A isotherms and spectroscopic changes during cycles. The extrapolated area per repeating unit of 240 Å^2 for **2** is the same as for **1**, confirming the face-on structure. A distinct difference of the P–A isotherm of **2** is the transition between 15 and 20 mN m^{-1}, when the orientation of the C repeating units change to an edge-on structure, allowing further compression up to 90 Å^2. We refer to **2**'s new alternating face-on and edge-on conformation (with neighbouring chains interlocked) as a zipper structure (Fig. 1). The areas per repeating unit predicted by molecular modelling are 196 Å^2 and 134 Å^2 for the face-on and the zipper structure respectively, which are in good agreement with the P–A isotherm (Fig. 2). The transition point (140 Å^2) in the P–A isotherm was calculated from the second derivative of the isotherm.

The spectroscopic measurements also support this zipper structure. Initial compression up to 15 mN m^{-1} causes the same minor perturbation of the π-conjugation system as in the case of **1**. However, continued compression from 15 to 20 mN m^{-1} causes a transition from the face-on to the zipper structure, which decreases the π-conjugation length thereby generating a large (21-nm) blue shift. A 34-nm blue shift is observed over the entire compression (0–20 mN m^{-1}). The fluorescence spectrum also showed a 9-nm blue shift with the face-on to zipper transition. The 38% increase in quantum yield is probably due to a larger energy gap and reduced intramolecular dynamics in the compressed state. The larger energy separation of the lowest singlet excited state, S_1, and the ground state S_0, decreases the Franck–Condon overlaps of the nuclear wavefunctions that control the internal conversion rate, and therefore an improved quantum yield is expected[16]. It is also possible that an interlocked zipper structure, which lacks extended π-conjugation, reduces the exciton's diffusion length thereby reducing quenching with molecular oxygen or other impurities. The λ_{max} of the initial face-on structure is red-shifted by 38 nm relative to solution,

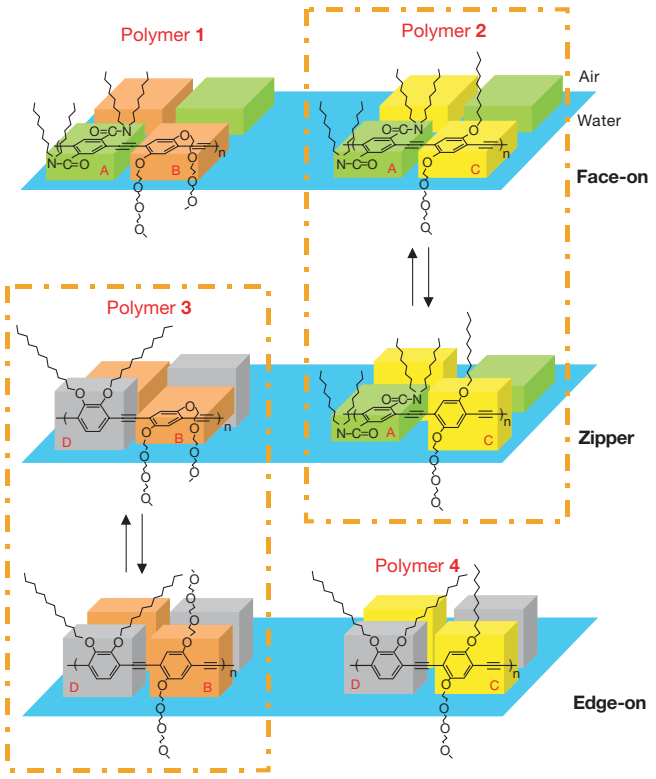

Figure 1 Conformations and spatial arrangements of polymers **1**–**4** at the air–water interface and their reversible conversions between face-on, zipper and edge-on structures. Polymer **1**: number-average molecular mass M_n = 23,000, Poly-dispersity index, PDI = 2.4. Polymer **2**: M_n = 293,000, PDI = 1.7. Polymer **3**: M_n = 115,000, PDI = 2.2. Polymer **4**: M_n = 96,000, PDI = 2.8. The monomers A, B, C and D are represented by green, orange, yellow and grey boxes, respectively.

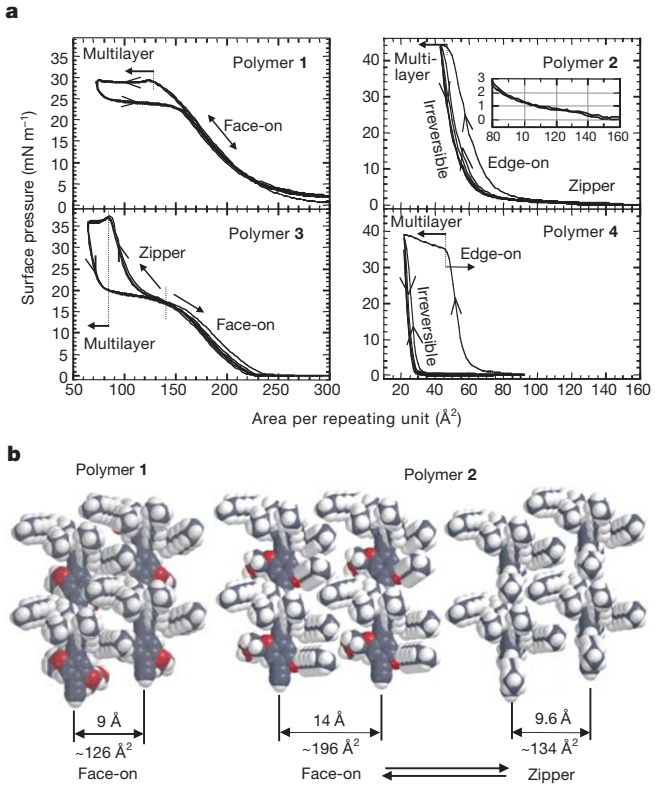

Figure 2 Pressure–area (P–A) isotherms of polymers **1**–**4** and projected areas from molecular models. **a**, P–A isotherms. **b**, Molecular models of adjacent polymer packing. Top views of two repeating units of polymers **1** and **2** are shown. The calculated length of one repeating unit is 14 Å, which is used to calculate the area per repeating unit from the modelling.

indicating, as mentioned earlier, that a non-planar conformation similar to the zipper structure is present in solution. The blue-shifted fluorescence λ_{max} of the zipper phase (462 nm) is also similar to the solution value (457 nm). The zipper structure is further supported by the synthesis of polymers with small amounts of ethynylene homo-coupling (that is, diacetylene groups) that disrupt the interlocking structure of polymer chains. A regularly alternating -A-C-A-C-A-C- structure is required to observe clear transitions in the P–A isotherm. Small amounts of an -A-C-C-A-C- imperfection[17] gives a less-featured P–A isotherm. After a monolayer of **2** folds into a multilayer film, a similar behaviour to that of **1** is observed, with the formation of an aggregation peak at 470 nm.

Langmuir monolayers of polymer **3** appear to assemble into the zipper structure before compression, and have an extrapolated area per repeating unit of 150 Å^2 that is much smaller than that of **1** and **2**. This zipper structure is promoted by the phenyl ring of building block D, which, when orientated normal to the surface, minimizes contact between the two hydrophobic sidechains and the water. The shape and λ_{max} of **3**'s uncompressed monolayer absorption and fluorescence spectra are consistently the same as those in solution. As **3** is compressed, one of the moderately hydrophilic triethylene-oxide groups from building block B is removed from the aqueous phase, and the film transforms from a zipper to an edge-on structure between 150 and 100 Å^2. This structural transition is probably facilitated by favourable interpolymer dipolar interactions between these polar side chains in the edge-on structure.

In the edge-on structure polymer **3** is co-facially arranged, and—as we have previously established—π-aggregation between main chains generates a new aggregation band in the UV–vis (Fig. 3a) spectra. This new narrow red-shifted band with a distinct shoulder is characteristic of a π-aggregated state with lower quantum yields, and should be distinguished from the red-shift owing to planarization alone[18] observed for **1** and **2**. The film in an edge-on structure is aggregated before film collapse; therefore no new band arises upon folding into a multilayer. As the aggregation band in the UV–vis. spectra grows the fluorescence is quenched, and when completely aggregated the quantum yield drops to 16% of the initial non-aggregated value (Fig. 3b). Before the folding of the monolayer into multilayers, the transition from the zipper to the edge-on structure is completely reversible. Therefore, releasing the surface pressure de-aggregates the film, and the initial absorbance and fluorescence spectra are re-established.

Polymer **4** has two edge-on building blocks, and forms the edge-on structure even before compression. Molecular modelling for **3** and **4** in an edge-on structure predicts an area per repeating unit of 64 Å^2, which is consistent with the value of 60 Å^2 from the P–A isotherm. As the film is compressed, the fluorescence intensity gradually decreases because the reduced distance between co-facially arranged polymer main chains promotes self-quenching[19,20]. The area per repeating unit at which the monolayer folds into

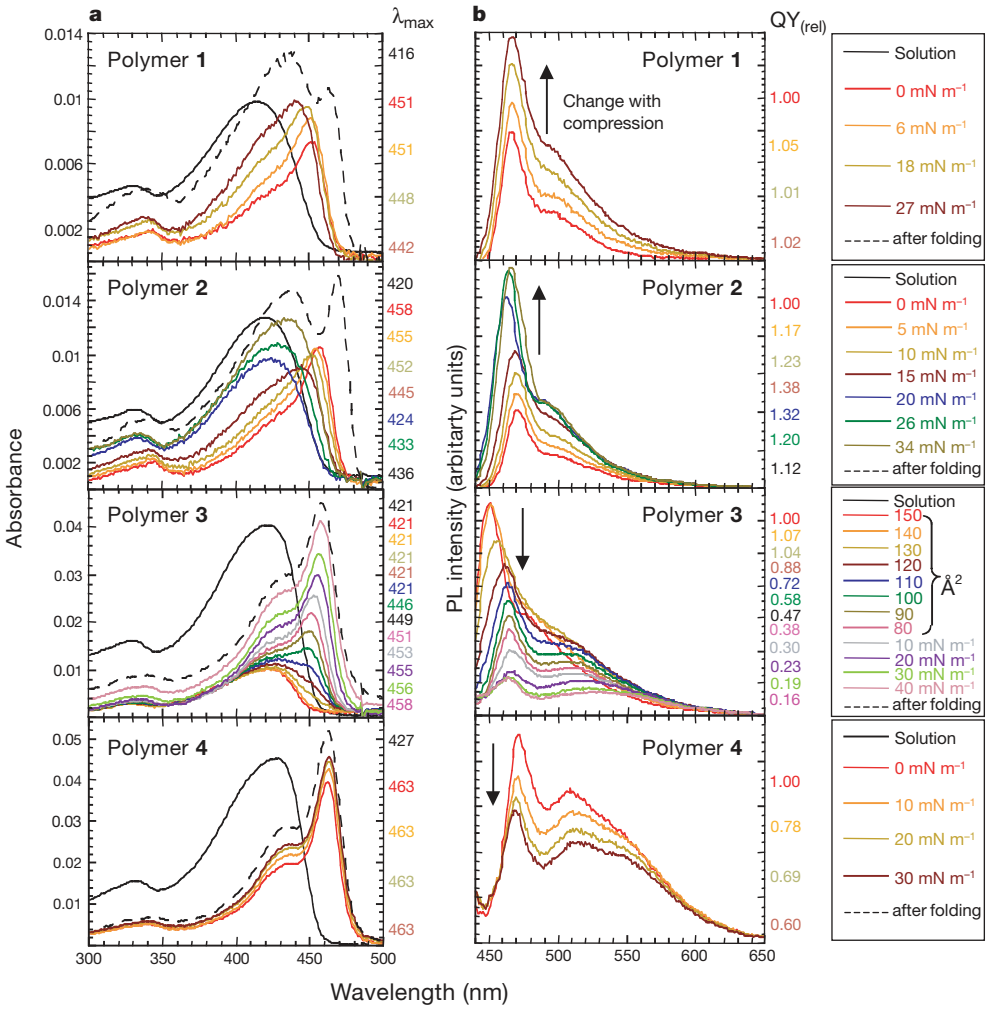

Figure 3 *In situ* UV–vis. and fluorescence spectra of Langmuir monolayers of polymers **1**–**4** during cycles of compressions and expansions. Polymer solutions were prepared in chloroform. **a**, *In situ* UV–vis. spectra and λ_{max} at various surface pressures. **b**, *In situ* fluorescence spectra and relative quantum yields (QY_{rel}) at various surface pressures and area per repeating units (relative quantum yield at 0 mN m^{-1} = 1). Excitation wavelength was 420 nm.

multilayers is 50 Å^2, the same value as for polymer **3**. This observation also supports the transition of **3** from the zipper to the edge-on. The aggregate emission bands are also identical with those of highly compressed **3**. The aggregate features are present at an area per repeating unit of 60 Å^2. This value and a repeat unit length of 14 Å provide an interpolymer distance of 4.3 Å, provided that the phenyl rings are standing perpendicular to the air–water interface. At higher pressures the emission is further quenched, and at the maximum compression of monolayers of polymers **3** and **4** the area per repeating unit is 50 Å^2, which provides an interpolymer spacing of 3.6 Å. The red-shifted absorption band implies that the aggregation is probably J-type. But because we have no knowledge of the registry of polymer chains with respect to each other, we cannot confirm whether the aggregation is of type H (in phase) or type J (out of phase).

To verify the nature of the emission peak at 471 nm and the sharp absorption peak at 463 nm for polymer **4**, we conducted non-solvent induced aggregation studies. Polymer **4** was dissolved in chloroform, and then UV–vis. and fluorescence spectra were taken as methanol, a non-solvent, was gradually added to the solution. Above equal amounts of chloroform and methanol, the polymer aggregates and absorption spectra display a pseudo-isosbestic point. (An isosbestic point implies that there are two different interconverting species.) Because of the limited solubility of **4**, it was technically difficult to conduct the experiment at a constant molar concentration, which is a necessary condition for a true isosbestic point. The absorption λ_{max} of the aggregate is 460 nm, close to the 463 nm of **4** at the air–water interface. The non-aggregated emission peak at 452 nm is continuously suppressed with added methanol until the spectrum has a main peak at 475 nm and two other peaks at about 510 and 545 nm. The final fluorescence spectrum is almost identical with the fluorescence spectrum of **4** in the edge-on structure at the air–water interface.

Excitation spectra of a solution in which an aggregated and a non-aggregated phase coexist have been collected by monitoring the emissions at 450, 475, 510 and 545 nm. The emission peak at 450 nm corresponds to the non-aggregated phase, as its excitation spectrum displays a maximum at 420 nm. The emission peaks at 475, 510 and 545 nm all have the same excitation spectra with peaks at 420 and 460 nm. Therefore, these three peaks are the result of polymer aggregates. The presence of the 420-nm peak in the excitation spectra is due to energy transfer from the higher-energy non-aggregated phase to the aggregated phase. We can discount the possibility of an excimer because we clearly see a ground-state absorption that is responsible for the new emission bands[21]. An excimer is an excited state complex, and should not result in new absorption bands. The lifetime of the non-aggregated band at 450 nm is 0.5 ns, and those of the other bands at 475, 510 and 545 nm are 0.1–0.2 ns. The lifetimes of excimers are often much longer than intrachain excitons[21], which also supports the fact that the longer-wavelength bands are not excimer peaks.

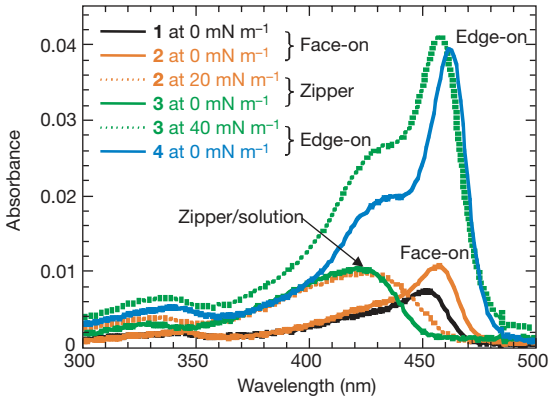

Figure 4 Selected UV–vis. spectra of polymers **1**–**4** in different structures (face-on, zipper, and edge-on). These data show the interrelationship between the conformation and interpolymer interactions.

Selected UV–vis. spectra of **1**–**4** from Fig. 3a are compared in Fig. 4. These spectra show the self-consistency of our results that have allowed us to unambiguously assign the structures to different spectral attributes. Polymers **1** and **2** have the same face-on structure at 0 mN m^{-1}; then mechanical pressure at 20 mN m^{-1} induces transition of **2** into the zipper structure—which **3** has initially at 0 mN m^{-1}. Mechanical compression of **3** causes the transition into the edge-on structure with a co-facial π-aggregation band that **4** has at 0 mN m^{-1}.

The combination of unique surfactant design and mechanical interrogation at the air–water interface have allowed us to show the interrelationships between the conformation of a single chain and the interpolymer interactions and a conjugated polymer's absorption and emission properties. Although these materials have been studied extensively[1–4,8,10–11,14], the intrinsic properties of isolated chains and ordered aggregates have yet to be established. The influence of structure on the charge- and energy-transporting properties of conjugated polymers could also be addressed by extensions of the methods presented here. □

Methods

A Nima 601 M model Langmuir–Blodgett trough with a window was used for the studies. The *in situ* UV–vis. spectra were obtained on a Hewlett-Packard 8453 diode array spectrophotometer or a Cary 50 Scan with fibre optics. The *in situ* fluorescence studies were conducted with a SPEX Fluorolog-τ2 fluorometer equipped with fibre optics. All the spectroscopic measurements on Langmuir films were conducted through optical fibres. Molecular modelling was performed using the Spartan 5.0 molecular modelling program (Wavefunction Inc, Irvine, California) running on a SGI O2 (R12000) workstation. These calculations are intended to give good estimates of the areas per repeating unit and required some geometric constraints that simulate the organizational preferences at the air–water interface.

Received 8 February; accepted 13 April 2001.

1. Nguyen, T.-Q., Wu, J., Doan V., Schwartz, B. J. & Tolbert, S. H. Control of energy transfer in oriented conjugated polymer-mesoporous silica composites. *Science* **288,** 652–656 (2000).
2. Shi, Y., Liu, J. & Yang, Y. Device performance and polymer morphology in polymer light emitting diodes: The control of thin film morphology and device quantum efficiency. *J. Appl. Phys.* **87,** 4254–4263 (2000).
3. Nguyen, T.-Q., Martini, I. B., Liu, J. & Schwartz, B. J. Controlling interchain interactions in conjugated polymers: The effects of chain morphology on exciton-exciton annihilation and aggregation in MEH-PPV films. *J. Phys. Chem. B* **104,** 237–255 (2000).
4. Sirringhaus, H. *et al.* Two-dimensional charge transport in self-organized, high-mobility conjugated polymers. *Nature* **401,** 685–688 (1999).
5. Lucht, B. L., Mao, S. S. H. & Tilley, T. D. A zirconocene-coupling route to substituted poly(*p*-phenylenedienylene)s: Band gap tuning via conformational control. *J. Am. Chem. Soc.* **120,** 4354–4365 (1998).
6. Cornil, J., dos Santos, D. A., Crispin, X., Silbey, R. & Brédas, J. L. Influence of interchain interactions on the absorption and luminescence of conjugated oligomers and polymers: A quantum-chemical characterization. *J. Am. Chem. Soc.* **120,** 1289–1299 (1998).
7. Yang, J.-S. & Swager, T. M. Fluorescent porous polymer films as TNT chemosensors: Electronic and structural effects. *J. Am. Chem. Soc.* **120,** 11864–11873 (1998).
8. Buvat, P. & Hourquebie, P. Enhanced infrared properties of regioregular poly(3-alkylthiophenes). *Macromolecules* **30,** 2685–2692 (1997).
9. Jenekhe, S. A. & Osaheni, J. A. Excimers and exciplexes of conjugated polymers. *Science* **265,** 765–768 (1994).
10. Gettinger, C. L., Heeger, A. J., Drake, J. M. & Pine, D. J. A photoluminescence study of poly(phenylene vinylene) derivatives—The effect of intrinsic persistence length. *J. Chem. Phys.* **101,** 1673–1678 (1994).
11. Heun, S. *et al.* Conformational effects in poly(*p*-phenylene vinylene)s revealed by low-temperature site-selective fluorescence. *J. Phys. Condens. Matter* **5,** 247–260 (1993).
12. Kim, J., McHugh, S. K. & Swager, T. M. Nanoscale fibrils and grids: Aggregated structures from rigid-rod conjugated polymers. *Macromolecules* **32,** 1500–1507 (1999).
13. Josefowicz, J. Y. *et al.* Structure of Langmuir-Blodgett films of disk-shaped molecules determined by atomic force microscopy. *Science* **260,** 323–326 (1993).
14. Zhang, Q. T. & Tour, J. M. Imine-bridged planar poly(phenylenethiophene)s and polythiophenes. *J. Am. Chem. Soc.* **119,** 9624–9631 (1997).
15. Levitsky, I. A., Kim, J. & Swager, T. M. Energy migration in a poly(phenylene ethynylene): determination of interpolymer transport in anisotropic Langmuir-Blodgett films. *J. Am. Chem. Soc.* **121,** 1466–1472 (1999).
16. Turro, N. J. *Modern Molecular Photochemistry* 183 (University Science Books, Sausalito, California, 1991).
17. Kloppenburg, L., Jones, D. & Bunz, U. H. F. High molecular weight poly(p-phenyleneethynylene)s by alkyne metathesis utilizing "instant" catalysts: A synthetic study. *Macromolecules* **32,** 4194–4203 (1999).

18. Miteva, T., Palmer, L., Kloppenburg, L., Neher, D. & Bunz, U. H. F. Interplay of thermochromicity and liquid crystalline behavior in poly(*p*-phenyleneethynylene)s: π-π interactions or planarization of the conjugated backbone? *Macromolecules* **33,** 652–654 (2000).
19. McQuade, D. T., Kim, J. & Swager, T. M. Two-dimensional conjugated polymer assemblies: Interchain spacing for control of photophysics. *J. Am. Chem. Soc.* **122,** 5885–5886 (2000).
20. Kim, J., McQuade, D. T., McHugh, S. K. & Swager, T. M. Ion-specific aggregation in conjugated polymers: Highly sensitive and selective fluorescent ion chemosensors. *Angew. Chem. Int. Edn Engl.* **39,** 3868–3872 (2000).
21. Cronwell, E. Excimer formation and luminescence in conducting polymers. *Trends Polym. Sci.* **5,** 218–222 (1997).

Supplementary information is available on *Nature*'s World-Wide Web site (http://www.nature.com) or as paper copy from the London editorial office of *Nature*.

Acknowledgements

We thank Z. Zhu for providing 1,2-didodecyloxy-3,6-diethynylbenzene (building block D), and A. Rose for the lifetime measurements. This work was supported by the Office of Naval Research and Draper Laboratory.

Correspondence and requests for materials should be addressed to T.M.S. (e-mail: tswager@mit.edu).

Biodegradation of oil in uplifted basins prevented by deep-burial sterilization

A. Wilhelms*, S. R. Larter†, I. Head†, P. Farrimond†, R. di-Primio* & C. Zwach*

* *Norsk Hydro Research Centre, PO 7190, 5020 Bergen, Norway*
† *Fossil Fuels and Environmental Geochemistry Postgraduate Institute (NRG), University of Newcastle, Newcastle upon Tyne NE1 7RU, UK*

Biodegradation of crude oil by bacterial activity—which has occurred in the majority of the Earth's oil reserves[1]—is known to reduce greatly the quality of petroleum in reservoirs[2]. For economically successful prospecting for oil, it is therefore important to understand the processes and conditions in geological formations that lead to oil biodegradation. Although recent studies speculate that bacterial activity can potentially occur up to temperatures as high as 150 °C (refs 3, 4), it is generally accepted that effective petroleum biodegradation over geological timescales generally occurs in reservoirs with temperatures below 80 °C (ref. 2). This appears, however, to be at odds with the observation that non-degraded oils can still be found in reservoirs below this temperature. Here we compile data regarding the extent of oil biodegradation in several oil reservoirs, and find that the extensive occurrence of non-biodegraded oil in shallow, cool basins is restricted to those that have been uplifted from deeper, hotter regions of the Earth. We suggest that these petroleum reservoirs were sterilized by heating to a temperature around 80–90 °C during deep burial, inactivating hydrocarbon-degrading organisms that occur in the deep biosphere. Even when such reservoirs are subsequently uplifted to much cooler regions and filled with oil, degradation does not occur, implying that the sterilized sediments are not recolonized by hydrocarbon-degrading bacteria.

Biodegradation of oil leads to a systematic decrease in paraffin content and an increase in oil density, sulphur content, acidity and viscosity[2], with negative economic consequences for oil production and refining operations. So prediction of the degree of biodegradation of oil is important for assessing the risk of finding degraded oils in an exploration target before drilling. The details and rates of the processes involved in crude-oil degradation are still poorly understood, but the central role of bacteria in subsurface petroleum degradation is accepted. Although there is abundant evidence for the presence of active bacteria deep (>1 km) in the Earth's crust[3,5–7], and a view among biologists that life in deep sediments may occur even up to 150 °C (refs 3, 4), there is a general view today among petroleum geoscientists that biodegradation in reservoirs ceases around 75–80 °C (refs 2, 8) in the zone of thermophilic organisms.

Hyperthermophilic organisms grow best above 80 °C, and have been reported to live at temperatures of up to 113 °C (ref. 9), but often display no growth below 60 °C (ref. 4). Most reports of hyperthermophilic activity are limited to environments rich in reduced electron donors, electron acceptors and inorganic nutrients necessary for biosynthesis—environments typically associated with shallow sediment or near-surface hydrothermal activity[10], where high levels of metabolic activity can be supported. Although petroleum reservoirs are rich in reduced organic electron donors (hydrocarbons), most petroleum reservoirs and deep aquifers are nutrient depleted[11] and recent studies indicate that biodegradation of petroleum in deep reservoirs is occurring at very slow net rates, typically consuming around 10^{-6} mmol oil per litre per day (ref. 12). These are similar to the respiration rates suggested for other deep sediments, and several orders of magnitude slower than respiration rates in anaerobic laboratory or near-surface sediment environments[11,13,14]. As electron donor (oil) supply is not limiting, degradation is presumably nutrient limited. Under these stressed, nutrient-limited conditions, it is unlikely that the temperature extremes survived by organisms in nutrient-rich hydrothermal environments are relevant. Furthermore, the empirical upper temperature limit of 80 °C observed for petroleum biodegradation in deep reservoirs is considerably lower than temperatures quoted for the denaturation and decomposition of many bacterial and archaeal proteins and nucleic acids[9,15]; this implies that active hyperthermophilic hydrocarbon-degraders are probably not present in petroleum reservoirs. Indeed, the single report of a hyperthermophilic archaeon that grew in enrichment cultures with crude oil as sole source of carbon[16] did not provide unequivocal evidence that the hyperthermophiles isolated could degrade hydrocarbons.

Although the occurrence of hyperthermophiles in petroleum reservoirs is now well documented[17–21], only four isolates capable of growth at greater than 90 °C have been reported[16–19]. In the most extreme of these cases (growth at 102 °C), evidence was presented that suggested that the organisms concerned may have originated from hydrothermal vent systems and were introduced with injected sea water[16]. The other cases where hyperthermophiles have been isolated are also sea-water-flooded reservoirs[19]. For the most part, microbial enrichments from petroleum reservoir samples conducted at temperatures above 85 °C have been unsuccessful[19,21], with increasing success of enrichment cultures with decreasing growth temperature (reaching 77% ($n = 26$) at temperatures below 60 °C)[19]. We also note that the only thermophilic anaerobic bacterium for which hydrocarbon degradation has been unequivocally demonstrated (an anaerobic sulphate-reducer) has an optimum growth temperature of only 60 °C (ref. 22). It has also been found that enrichment cultures supplied with crude oil as the sole source of organic carbon at temperatures greater than 85 °C failed to produce cultures of putative hydrocarbon-degrading Archaea although hyperthermophiles that grow at temperatures up to 102 °C could be isolated[16]. Taken together, data from most reports of Bacteria and Archaea isolated from petroleum reservoirs support the notion that the organisms which inhabit these reservoirs do not thrive in the upper temperature ranges for hyperthermophiles (up to 113 °C), and show little indication of hydrocarbon degrading capacity above 80 °C. We realize, however, that any interpretation must be viewed cautiously (as most reports provide little information on failed enrichments, and recent experience in defining the limits of life warn of inherent difficulty in definitively excluding life processes from even severe environments).

Biodegraded oils are common in cool (<80 °C), shallow reservoirs in currently subsiding basins such as those in the North Sea,

11. Hebert, P. D. N. & Emery, C. J. The adaptive significance of cuticular pigmentation in *Daphnia*. *Funct. Ecol.* **4,** 703–710 (1990).
12. Lampert, W. The adaptive significance of diel vertical migration of zooplankton. *Funct. Ecol.* **3,** 21–27 (1989).
13. De Meester, L., Dawidowicz, P., van Gool, E. & Loose, C. J. in *The Ecology and Evolution of Inducible Defenses* (eds. Tollrian, R. & Harvell, C. D.) 160–176 (Princeton Univ. Press, Princeton, New Jersey, 1999).
14. Ringelberg, J. The positively phototactic reaction of *Daphnia magna* Strauss: a contribution to the understanding of diurnal vertical migration. *Neth. J. Sea Res.* **2,** 319–406 (1964).
15. Bollens, S. M., Frost, B. W. & Cordell, J. R. Chemical, mechanical and visual cues in the vertical migration behavior of the marine planktonic copepod *Acartia hudsonica*. *J. Plankton Res.* **16,** 555–564 (1994).
16. Loose, C. J. & Dawidowicz, P. Trade-offs in diel vertical migration by zooplankton: The costs of predator avoidance. *Ecology* **75,** 2255–2263 (1994).
17. Fleischmann, E. M. The measurement and penetration of ultraviolet radiation into tropical marine water. *Limnol. Oceanogr.* **34,** 1623–1629 (1989).
18. Morris, D. P. *et al.* The attenuation of solar UV radiation in lakes and the role of dissolved organic carbon. *Limnol. Oceanogr.* **40,** 1381–1391 (1995).
19. Smith, K. C. & Macagno, E. R. UV photoreception in the compound eye of *Daphnia magna* (Crustacea, Branchiopoda). A fourth spectral class in single ommatidia. *J. Comp. Physiol. A* **166,** 597–606 (1990).
20. Merker, E. Sehen die Daphnien ultravioletten Licht? *Zool. Jahrb. Abt. Allg. Zool. Physiol. Tiere.* **48,** 277–348 (1930).
21. Hessen, D. O. *Daphnia* responses to UV-light. *Arch. Hydrobiol. Beih.* **43,** 85–195 (1994).
22. Storz, U. C. & Paul, R. J. Phototaxis in water fleas (*Daphnia magna*) is differently influenced by visible and UV light. *Comp. Physiol. A* **183,** 709–717 (1998).
23. Leech, D. M. & Williamson, C. E. *In situ* exposure to ultraviolet radiation alters the depth distribution of *Daphnia*. *Limnol. Oceanogr.* **46,** 416–420 (2001).
24. Damkaer, D. M. in *The Role of Solar Ultraviolet Radiation in Marine Ecosystems* (ed. Calkins, J.) 701–706 (Plenum, New York, 1982).
25. Dodson, S. I. Predicting diel vertical migration of zooplankton. *Limnol. Oceanogr.* **35,** 1195–1200 (1990).
26. Smith, R. C. & Baker, K. S. Optical properties of the clearest natural waters (200–800 nm). *Appl. Optics* **20,** 177–184 (1981).
27. Vinyard, G. L. & O'Brien, W. J. Effects of light and turbidity on the reactive distance of bluegill (*Lepomis macrochirus*). *J. Fish. Res. Bd. Can.* **33,** 2845–2849 (1976).
28. Confer, J. L. *et al.* Visual predation by planktivores. *Oikos* **31,** 27–37 (1978).
29. Madronich, S., McKenzie, R. L., Caldwell, M. M. & Bjorn, L. Changes in ultraviolet radiation reaching the earth's surface. *Ambio* **24,** 143–152 (1995).

Acknowledgements

We thank L. J. Weider for providing arctic *D. pulex*. We also thank A. Agrawal, W. Gabriel, S. Gieβler, A. F. Sell, B. Schierwater, T. Vines, C. E. Williamson, W. C. Kerfoot and L. J. Weider for comments and advice on earlier versions of the manuscript.

Correspondence and requests for materials should be addressed to R.T. (e-mail: ralph.tollrian@lrz.uni-muenchen.de).

Partitioning selection and complementarity in biodiversity experiments

Michel Loreau* & Andy Hector†

** Laboratoire d'Écologie, UMR 7625, École Normale Supérieure, 46 rue d'Ulm, 75230 Paris Cedex 05, France*
† NERC Centre for Population Biology, Imperial College at Silwood Park, Ascot, Berkshire SL5 7PY, UK

The impact of biodiversity loss on the functioning of ecosystems and their ability to provide ecological services has become a central issue in ecology. Several experiments have provided evidence that reduced species diversity may impair ecosystem processes such as plant biomass production[1–5]. The interpretation of these experiments, however, has been controversial[6–12] because two types of mechanism may operate in combination[6,13–15]. In the 'selection effect', dominance by species with particular traits affects ecosystem processes. In the 'complementarity effect', resource partitioning or positive interactions lead to increased total resource use. Here we present a new approach to separate the two effects on the basis of an additive partitioning analogous to the Price equation in evolutionary genetics[16–19]. Applying this method to data from the pan-European BIODEPTH experiment[4] reveals that the selection effect is zero on average and varies from negative to positive in different localities, depending on whether species with lower- or higher-than-average biomass dominate communities. In contrast, the complementarity effect is positive overall, supporting the hypothesis that plant diversity influences primary production in European grasslands through niche differentiation or facilitation.

Recent theoretical work has revealed that the observed responses of ecosystem processes to changes in species or functional-group diversity can be generated by a combination of different effects[13–15]. These biodiversity effects can be grouped into two classes. First, there are those that arise from niche differentiation or facilitation between species, and that can increase the performance of communities above that expected from the performance of individual species. Distinguishing the effects of niche differentiation and facilitation may often be difficult in practice; therefore, we refer to these mechanisms collectively as 'complementarity'. One common form of complementarity in plant communities (which involves both resource partitioning and facilitation) arises between legumes, which have the ability to fix atmospheric nitrogen, and other plants, which have access only to soil nitrogen.

The second class of biodiversity effects gives rise to relationships between biodiversity and ecosystem functioning through selective processes, such as interspecific competition, which cause dominance (high relative abundance) of species with particular traits. For example, in one model of the 'sampling effect'[6,13], higher-diversity plant mixtures assembled at random from a pool of species have a higher chance of containing and becoming dominated by the

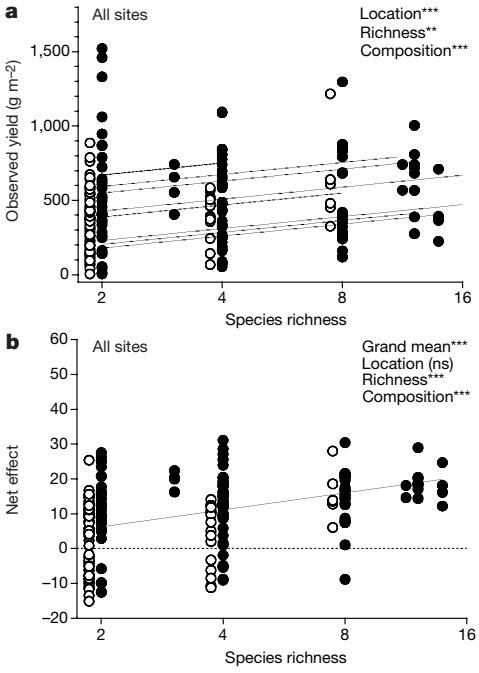

Figure 1 Observed yield Y_0 and net biodiversity effect ΔY as functions of species richness across all localities in mixtures of the BIODEPTH experiment. **a**, Observed yield; **b**, net biodiversity effect. Open circles are plots that do not contain any legume species; filled circles are plots that contain legumes. Lines are slopes from the multiple regression model using species richness on a $\log_2$ scale. Lines in **a** from highest elevation to lowest are: Germany, Silwood, Sheffield, Switzerland, Ireland, Greece, Sweden and Portugal. Values of the biodiversity effect (in g m^{-2}) are square-root transformed to meet the assumptions of analyses but preserve the original positive and negative signs. (Single asterisk, $P < 0.05$; double asterisk, $P < 0.01$; triple asterisk, $P < 0.001$; ns: non-significant.)

species that achieves the highest biomass when grown alone. The model assumes that the biomass of a mixture of species is equal to the monoculture biomass of the most productive of the component species.

Although both types of effect are potentially relevant, they have different implications and may apply to different circumstances[15].

Box 1

Additive partition of biodiversity effects

We measure the net biodiversity effect, ΔY, by the difference between the observed yield of a mixture and its expected yield under the null hypothesis that there is no selection effect or complementarity effect. This expected value is the weighted (by the initial relative abundance of species in mixture) average of the monoculture yields for the component species. Positive selection occurs if species with higher-than-average monoculture yields dominate the mixtures. The selection effect is measured by the covariance between the monoculture yield of species and their change in relative yield in the mixture. Finally, a positive complementarity effect occurs if species yields in a mixture are on average higher than expected on the basis of the weighted average monoculture yield of the component species. These various effects can be related by additive partition as follows.

Define, for any mixture,
M_i = yield of species i in monoculture
Y_{Oi} = observed yield of species i in the mixture
$Y_O = \Sigma_i Y_{Oi}$ = total observed yield of the mixture
RY_{Ei} = expected relative yield of species i in the mixture, which is simply its proportion seeded or planted
$RY_{Oi} = Y_{Oi}/M_i$ = observed relative yield of species i in the mixture
$Y_{Ei} = RY_{Ei}M_i$ = expected yield of species i in the mixture
$Y_E = \Sigma_i Y_{Ei}$ = total expected yield of the mixture
$\Delta Y = Y_O - Y_E$ = deviation from total expected yield in the mixture
$\Delta RY_i = RY_{Oi} - RY_{Ei}$ = deviation from expected relative yield of species i in the mixture
N = number of species in the mixture

It then follows that

$$\Delta Y = Y_O - Y_E = \sum_i RY_{Oi}M_i - \sum_i RY_{Ei}M_i = \sum_i \Delta RY_i M_i$$

$$= N\,\overline{\Delta RY}\,\overline{M} + N\,\mathrm{cov}(\Delta RY, M)$$

In this equation, $N\,\overline{\Delta RY}\,\overline{M}$ measures the complementarity effect, and $N\,\mathrm{cov}(\Delta RY, M)$ measures the selection effect.

Note that this approach is a generalization of the relative yield total (RYT) and proportional deviation from expected value (D) approaches[21,22]. Indeed, $N\,\overline{\Delta RY} = RYT - 1 = \overline{D}$ and $\Delta Y = D_T Y_E$. Thus, the above equation can be rewritten as $D_T Y_E = \overline{D}\,\overline{M} + N\,\mathrm{cov}(\Delta RY, M)$ from which it is apparent that the net biodiversity effect is proportional to D_T, and the complementarity effect is proportional to $\overline{D}$.

As a consequence, our method has similar strengths and limitations to these approaches. Relative yield has traditionally been used in short-term plant competition experiments with substitutive designs in which total density is kept constant (as was the case in BIODEPTH). Results may then be dependent on the chosen density[11,20], although they seldom vary strongly in practice[12,25]. Our approach, however, could be applied to other organisms and other experimental designs in which density is allowed to reach natural levels. As it is based on variation in relative yield (ΔRY), it could also be used to study how biodiversity effects change through time, by comparing observed values at each time with expected values calculated either from initial conditions or from the conditions of the previous time. □

Much of the controversy over recent experiments has revolved around the significance of the sampling effect and its contribution to the observed responses to experimental manipulations of biodiversity[6–12], prompting the need for methods to separate the sampling effect from complementarity[20–22]. The sampling effect model, however, has restrictive assumptions which do not qualify it as a general alternative to complementarity. First, communities may not be dominated by a single species, and relative abundance and the magnitude of impact on ecosystem functioning may not be positively correlated. In particular, a negative selection effect can arise if communities are dominated by species with low—not high—values for a particular trait or process[14,15,23]. Second, the sampling effect model actually combines two different processes: a sampling process and an extreme selection process that favours the single most productive species. The sampling process is shared by the selection and complementarity mechanisms: in both cases, communities that have more species also have a greater probability of containing the appropriate species (either single species with particular trait values or a combination of species with complementary traits). Thus selection, not sampling, really distinguishes the two classes of mechanism[15]. This strengthens the need for more general, conceptually clear methods that can identify their individual contributions in biodiversity experiments.

Our new methodological approach meets this need by providing an additive partitioning of two biodiversity effects: a 'selection effect' and a 'complementarity effect' (Box 1). The selection effect is based on Price's general theory of selection[24]: selection occurs when changes in the relative yields of species in a mixture are non-randomly related to their traits (yields) in monoculture. Accordingly, selection is measured by a covariance function as in the Price equation of evolutionary genetics[16–19]. The complementarity effect measures any change in the average relative yield in the mixture, whether positive (resulting from resource partitioning or facilitation) or negative (resulting from physical or chemical interference). The sum of these two effects is the net biodiversity effect; it measures the deviation of the mixture yield from its expected value on the basis of monoculture yields and the relative abundance of species in the mixtures. All three effects have the dimension of yield (where yield is a surrogate for any measurable ecosystem property), and an expected value of zero under the null hypothesis of no biodiversity effect. Consequently, all three can equally be positive or negative, and there is a potential for complementarity and selection effects to cancel each other, resulting in a zero net effect. Our additive partition unifies and relates in a single equation previous measures based on the relative yield total and proportional deviation from expected value approaches (Box 1). Another advantage over previous methods is that our additive partition provides absolute measures of biodiversity effects, thereby allowing quantitative comparison of their respective contributions.

We applied this methodology to patterns of aboveground biomass production obtained from the BIODEPTH project, a network of field experiments that examined the functioning of European grassland ecosystems in relation to the direct manipulation of plant diversity[4]. As our approach requires a comparison between the performances of species in mixture and in monoculture, we restricted its application to the subset of experimental mixture plots that contained species for which monoculture yields were available. The overall pattern for this subset was similar to that for the whole experiment[4]: a log-linear increase in aboveground biomass with species richness and a significant locality effect, but no significant interaction between species richness and locality (Fig. 1a). The net biodiversity effect was positive (the grand mean was significantly different from zero) and increased significantly with species richness beyond two species (Fig. 1b; Table 1). Species composition always had a significant effect.

The two components of this net effect, selection and complementarity, had strikingly different patterns. The selection effect

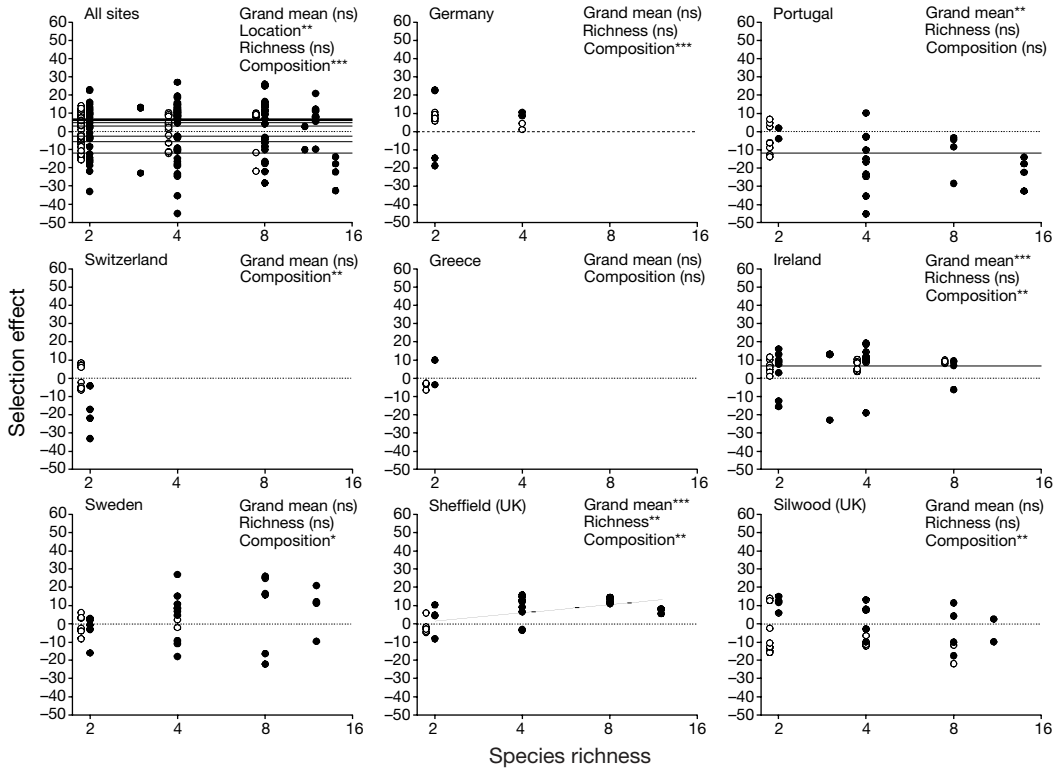

Figure 2 Selection effect, $N\,\mathrm{cov}(\Delta \mathrm{RY}, M)$, as a function of species richness across all localities and at individual localities. Lines from highest elevation to lowest are: Ireland, Germany, Sheffield, Greece, Sweden, Silwood, Switzerland and Portugal. Values are square-root transformed to meet the assumptions of analyses but preserve the original positive and negative signs. Symbols as in Fig. 1.

was variable, ranging from significantly positive averages in two localities (Ireland and Sheffield) to a significantly negative average in one locality (Portugal) (Fig. 2). Overall, across all sites, these variations cancelled out, so that the grand mean was not significantly different from zero, and selection was unaffected by species richness. The only factors that influenced selection significantly were locality and species composition (Fig. 2; Table 1).

In contrast, the average complementarity effect was significantly positive in four localities (Portugal, Ireland, Sheffield and Silwood) and in the overall analysis across site (Fig. 3; Table 1). Furthermore, complementarity increased significantly with the species richness of mixtures in two localities (Sheffield and Portugal) and across all localities. There were again significant locality and composition effects, but no significant locality-by-species richness interaction (Table 1). Thus, the best statistical model for the overall across-site analysis was a log-linear relationship between complementarity and species richness with identical slopes but different heights in the various localities (Fig. 3).

One particular form of complementarity occurs between nitrogen-fixing legumes and other plants. Might the fertilization effect of legumes be sufficient to explain the positive complementarity effect found in this experiment[11]? The presence of legumes in the mixtures did have important impacts on their performance; in general it tended to increase yields as well as the net and complementarity effects, and to generate more extreme selection effects, whether positive or negative (Figs 1–3). Although the experiment was not designed to fully separate the effects of legumes or functional-group diversity from that of species diversity, our method can also be applied to examine this issue. When the presence of legumes was included as an additional factor in our across-site analyses, species richness—in addition to locality, presence of legumes and species composition—retained a significant log-linear effect on complementarity, whether legumes were introduced after ($F_{(1,67)} = 11.36$, $P < 0.01$) or before ($F_{(1,67)} = 4.74$, $P < 0.05$)

Table 1 Summary of the analysis of biodiversity effects for mixtures of the BIODEPTH experiment

		Net effect, ΔY			Selection effect, $N\,\mathrm{cov}(\Delta \mathrm{RY}, M)$			Complementarity effect, $N\,\Delta \mathrm{RY}\,M$		
	d.f.	MS	F	P	MS	F	P	MS	F	P
Grand mean	1	20,000.65	129.30	2.63×10^{-18}	257.78	1.44	0.2334	15,830.07	87.74	1.87×10^{-14}
Locality	7	224.09	1.45	0.1980	1,267.88	7.09	0.0094	606.99	3.36	0.0034
Species richness ($\log_2$)	1	3,210.81	20.76	1.87×10^{-5}	23.35	0.13	0.7188	1,879.89	10.42	0.0018
Deviation	5	76.61	0.50	0.7789	133.54	0.75	0.5908	177.04	0.98	0.4346
Locality × richness	5	203.89	1.32	0.2650	340.27	1.90	0.1031	110.68	0.61	0.6898
Composition	79	154.68	4.41	1.14×10^{-12}	178.79	3.13	2.59×10^{-8}	180.42	1.99	0.0005
Residual	107	35.06			57.13			90.69		
Total	205									

All terms were tested against the average variation between replicate mixtures—the Composition term—and composition effects against the overall residual (mixture-by-block interaction). The first line reports a test of the grand mean effects across all mixtures versus the null expectation of zero and subsequent lines test for effects of location and diversity. Data were square-root transformed while preserving the original positive or negative signs to meet the assumptions of analyses. d.f., degrees of freedom; MS, mean squares.

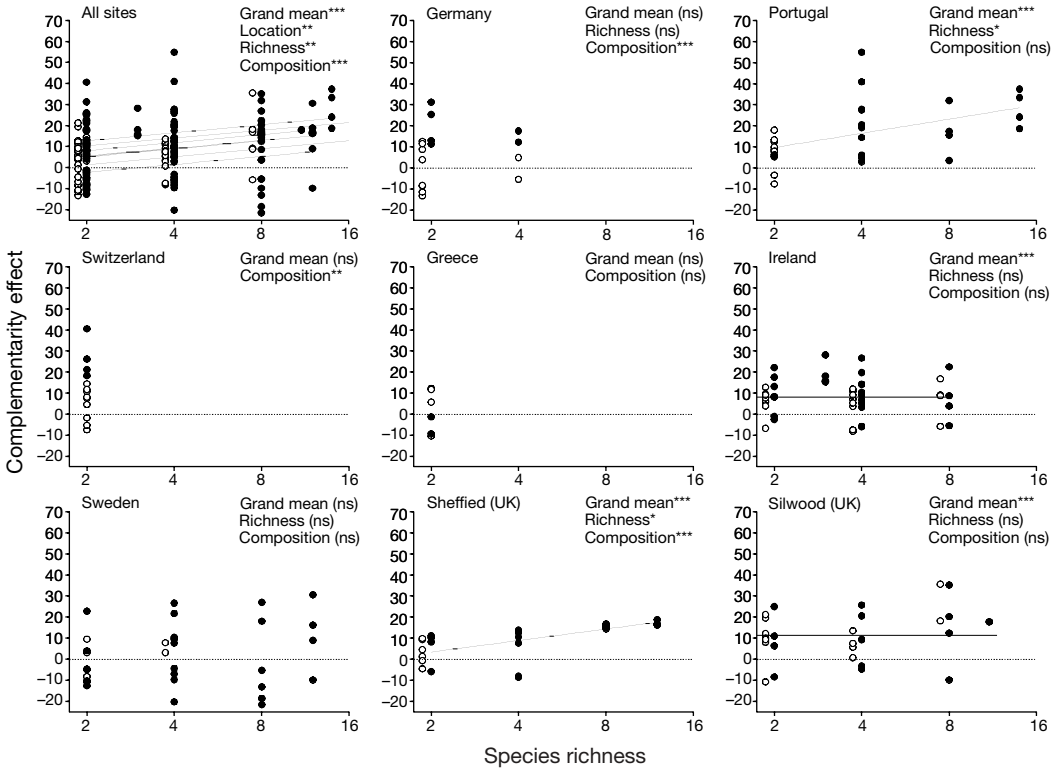

Figure 3 Complementarity effect, $N\overline{\Delta RY}\,\overline{M}$, as a function of species richness across all localities and at individual localities. Lines from highest elevation to lowest are: Portugal, Switzerland, Silwood, Germany, Sheffield, Ireland, Greece and Sweden. Values are square-root transformed to meet the assumptions of analyses but preserve the original positive and negative signs. Symbols as in Fig. 1.

species richness. The latter test was very conservative as the presence of legumes was embedded within species richness in the experiment, so that part of the species richness effect was absorbed into the legume effect when it was fitted first in the analysis. Thus, the increased complementarity in species-rich mixtures involved not only complementarity between legumes and other plant types, but also complementarity between species within each of these groups.

Our analysis confirms theoretical predictions that selection effects should be more variable and less predictable than complementarity[14,15]. In the BIODEPTH experiment, selection favoured species with either high or low monoculture yield depending on locality, and did not contribute to aboveground biomass patterns across localities. Therefore the selection effect can be rejected as the sole mechanism explaining the results from this experiment. In contrast, although complementarity was also variable, it was consistently positive overall and presented the same log-linear dependency on species richness as did the raw and net biodiversity effects. Furthermore, this dependence involved both complementarity between nitrogen-fixing legumes and other species, and complementarity between species within each group. Therefore, our analysis supports the hypothesis that plant diversity influences primary production in European grasslands at least partly through some combination of niche differentiation and facilitation between species[4].

Our methodology provides a powerful means to *a posteriori* partition the selection and complementarity components of biodiversity effects in biodiversity–ecosystem functioning experiments. Our measure of complementarity, however, is linearly related to the relative yield total and, therefore, has similar strengths and limitations (Box 1). It cannot replace direct experimental investigations into the mechanisms at work in responses to biodiversity changes at the ecosystem level, which are now critical to further progress in this area. □

Methods

Experimental data

The BIODEPTH experiment simulated the loss of plant species in grassland ecosystems by removing the existing vegetation and seed bank and re-establishing plant communities from seed using standardized protocols at two localities in the UK (Sheffield and Silwood) and at single localities in Germany, Ireland, Greece, Portugal, Sweden and Switzerland. At each site, five levels of species richness were established, ranging from monocultures to higher diversity assemblages that approximately matched background levels of diversity in comparable unmanipulated semi-natural grasslands. To replicate plant diversity, each level of species richness was represented by several different plant assemblages at each site. Constrained random selection from the local pool of grassland species was used to form assemblages where all polycultures contained at least one grass. To investigate the effects of species composition, each assemblage was replicated in a minimum of two plots at each site including monocultures of many of the species involved. In total, the experiment comprised 480 plots, in which various ecosystem properties were measured. More details on the experimental design can be found elsewhere[4,12]. For our analysis, we used data on aboveground plant biomass production measured two years after establishment of the experimental plots, in the subset of polyculture plots for which all species were also grown in monoculture at the same site. This subset comprised 205 of the 308 polyculture plots.

Statistical analyses

Data were analysed by analysis of variance and linear regression. Initial (sown) species richness was used in the analysis because it defined treatments in the experimental design; realised species richness closely matched sown species richness and produced similar results[4,12]. Values of the selection, complementarity and net biodiversity effects were transformed to meet assumptions of tests by taking the square root while preserving the original sign (alternative transformations produced similar results). We tested two main hypotheses. First, we tested grand mean values across all polycultures versus zero to see whether they differed significantly from the weighted average of the monoculture yields. Second, we performed analysis of variance, partitioning the relationship into a linear regression, testing for positive or negative relationships with species richness above two species, and testing the deviation from this relationship. Details of similar analyses of the full set of 480 plots are available elsewhere[4,12].

Received 20 December; accepted 13 March 2001.

1. Tilman, D., Wedin, D. & Knops, J. Productivity and sustainability influenced by biodiversity in grassland ecosystems. *Nature* **379,** 718–720 (1996).
2. Tilman, D. *et al.* The influence of functional diversity and composition on ecosystem processes. *Science* **277,** 1300–1302 (1997).

3. van der Heijden, M. G. A. *et al.* Mycorrhizal fungal diversity determines plant biodiversity, ecosystem variability and productivity. *Nature* **396,** 69–72 (1998).
4. Hector, A. *et al.* Plant diversity and productivity experiments in European grasslands. *Science* **286,** 1123–1127 (1999).
5. Schläpfer, F. & Schmid, B. Ecosystem effects of biodiversity: a classification of hypotheses and exploration of empirical results. *Ecol. Appl.* **9,** 893–912 (1999).
6. Huston, M. A. Hidden treatments in ecological experiments: re-evaluating the ecosystem function of biodiversity. *Oecologia* **110,** 449–460 (1997).
7. Aarssen, L. W. High productivity in grassland ecosystems: effected by species diversity or productive species? *Oikos* **80,** 183–184 (1997).
8. Tilman, D. Distinguishing the effects of species diversity and species composition. *Oikos* **80,** 185 (1997).
9. Wardle, D. A. Is 'sampling effect' a problem for experiments investigating biodiversity–ecosystem function relationships? *Oikos* **87,** 403–407 (1999).
10. van der Heijden, M. G. A. *et al.* 'Sampling effect', a problem in biodiversity manipulation? A reply to David A. Wardle. *Oikos* **87,** 408–410 (1999).
11. Huston, M. A. *et al.* No consistent effect of plant diversity on productivity. *Science* **289,** 1255 (2000).
12. Hector, A. *et al.* No consistent effect of plant diversity on productivity: Response. *Science* **289,** 1255 (2000).
13. Tilman, D., Lehman, C. & Thompson, K. Plant diversity and ecosystem productivity: theoretical considerations. *Proc. Natl Acad. Sci. USA* **94,** 1857–1861 (1997).
14. Loreau, M. Biodiversity and ecosystem functioning: a mechanistic model. *Proc. Natl Acad. Sci. USA* **95,** 5632–5636 (1998).
15. Loreau, M. Biodiversity and ecosystem functioning: recent theoretical advances. *Oikos* **91,** 3–17 (2000).
16. Price, G. R. Selection and covariance. *Nature* **227,** 520–521 (1970).
17. Price, G. R. Extension of covariance selection mathematics. *Ann. Hum. Genet.* **35,** 485–490 (1972).
18. Frank, S. A. George Price's contributions to evolutionary genetics. *J. Theor. Biol.* **175,** 373–388 (1995).
19. Frank, S. A. The Price Equation, Fisher's fundamental theorem, kin selection, and causal analysis. *Evolution* **51,** 1712–1729 (1997).
20. Garnier, E., Navas, M.-L., Austin, M. P., Lilley, J. M. & Gifford, R. M. A problem for biodiversity–productivity studies: how to compare the productivity of multispecific plant mixtures to that of monocultures? *Acta Oecol.* **18,** 657–670 (1997).
21. Hector, A. The effect of diversity on productivity: detecting the role of species complementarity. *Oikos* **82,** 597–599 (1998).
22. Loreau, M. Separating sampling and other effects in biodiversity experiments. *Oikos* **82,** 600–602 (1998).
23. Troumbis, A. Y., Dimitrakopoulos, P. G., Siamantziouras, A.-S. D. & Memtsas, D. Hidden diversity and productivity patterns in mixed Mediterranean grasslands. *Oikos* **90,** 549–559 (2000).
24. Price, G. R. The nature of selection. *J. Theor. Biol.* **175,** 389–396 (1995).
25. Jolliffe, P. A. The replacement series. *J. Ecol.* **88,** 371–385 (2000).

Acknowledgements

We thank S. Yachi, B. Schmid and D. Deutschman for suggestions and all members of BIODEPTH for their input to the project. This work was supported by the CNRS GDR 1936 DIV-ECO and the CNRS PICS *Dynamics of biodiversity: from species interactions to ecosystem functioning*.

Correspondence and requests for materials should be addressed to M.L. (e-mail: Loreau@ens.fr).

Cryptic evolution in a wild bird population

J. Merilä*, L. E. B. Kruuk† & B. C. Sheldon‡§

* *Department of Population Biology, Evolutionary Biology Centre, Uppsala University, Norbyvägen 18d, SE-752 36 Uppsala, Sweden*
† *Institute of Cell, Animal and Population Biology, University of Edinburgh, Edinburgh EH9 3JT, UK*
‡ *Department of Zoology, University of Oxford, South Parks Road, Oxford OX1 3PS, UK*
§ *Department of Animal Ecology, Evolutionary Biology Centre, Uppsala University, Norbyvägen 18d, SE-752 36 Uppsala, Sweden*

Microevolution is expected to be commonplace, yet there are few thoroughly documented cases of microevolution in wild populations[1,2]. In contrast, it is often observed that apparently heritable traits under strong and consistent directional selection fail to show the expected evolutionary response[3,4]. One explanation proposed for this paradox is that a genetic response to selection may be masked by opposing changes in the environment[5,6]. We used data from a 20-year study of collared flycatchers (*Ficedula albicollis*) to explore selection on, and evolution of, a heritable trait: relative body weight at fledging ('condition'). Despite consistent positive directional selection, on both the phenotypic and the additive genetic component (breeding values, estimated from an animal model) of condition, the mean phenotypic value of this trait in the population has declined, rather than increased, over time. Here we show that, despite this decline, the mean breeding value for condition has increased over time. The mismatch between response to selection at the levels of genotype and phenotype can be explained by environmental deterioration, concealing underlying evolution. This form of cryptic evolution may be common in natural environments.

If selection acts consistently on a heritable trait in a population, it should, all else being equal, induce a permanent change in the distribution of that trait[7]. The frequent lack of expected evolutionary change in heritable traits under directional selection in the wild has therefore puzzled evolutionary biologists for some time. Explanations proposed to account for this paradox include: inflated estimates of heritability owing to environmental covariance between relatives[7], spatially and temporally varying selection pressures[8], negative genetic correlations between different components of fitness[8], and selection restricted to the environmental component of the phenotype[3,4]. Another possibility is that a genetic response to selection does in fact occur, but is masked by opposing changes in the environment[5,6]. However, to date, these alternatives have been subjected to very little empirical scrutiny[8].

In many passerine bird species, relative body mass (the condition index) is an important predictor of the survival of fledglings: relatively heavier nestlings are more likely to survive to become breeding adults[9–11]. This is also true for juvenile survival in other taxa, such as reptiles[12] and mammals[13]. In the collared flycatcher, quantitative genetic analyses using traditional methods suggest a

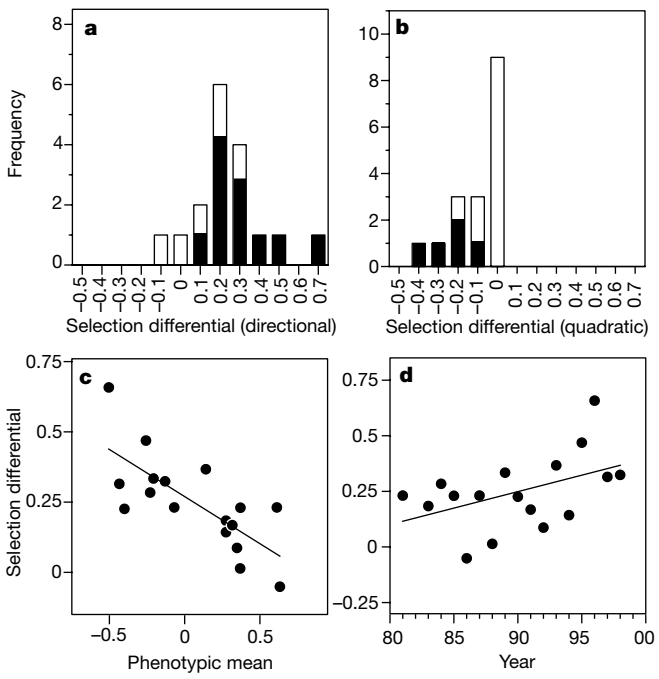

Figure 1 Patterns of natural selection on condition index of nestling collared flycatchers from 1981 to 1998. **a**, Distribution of directional standardized selection coefficients observed in each year. **b**, Distribution of quadratic standardized selection coefficients, with negative values indicating stabilizing selection. **c**, Relationship between mean condition index and intensity of directional survival selection across different study years. **d**, Intensity of directional survival selection on body condition index as a function of time. In **a** and **b**, the shaded proportions of bars indicate selection coefficients significantly ($P < 0.05$) different from zero.